Research Paper

GEOSPHERE

GEOSPHERE, v. 15, no. 4

https://doi.org/10.1130/GES02040.1

11 figures; 3 tables; 1 set of supplemental files

CORRESPONDENCE: chughe19@vols.utk.edu

CITATION: Hughes, C.A., Jessup, M.J., Shaw, C.A., and Newell, D.L., 2019, Deformation conditions during syn-convergent extension along the Cordillera Blanca shear zone, Peru: Geosphere, v. 15, no. 4, p. 1342–1367, https://doi.org/10.1130/GES02040.1.

Science Editors: Raymond M. Russo, Andrea Hampel
Associate Editor: Jose M. Hurtado

Received 21 July 2018
Revision received 21 December 2018
Accepted 25 March 2019

Published online 13 June 2019

Deformation conditions during syn-convergent extension along the Cordillera Blanca shear zone, Peru

Cameron A. Hughes[1], Micah J. Jessup[1], Colin A. Shaw[2], and Dennis L. Newell[3]

[1]Department of Earth and Planetary Sciences, University of Tennessee–Knoxville, 1621 Cumberland Avenue, 602 Strong Hall, Knoxville, Tennessee 37996-1526, USA
[2]Department of Earth Sciences, Montana State University, P.O. Box 173480, Bozeman, Montana 59717-3480, USA
[3]Department of Geology, Utah State University, 4505 Old Main Hill, Logan, Utah 84322, USA

ABSTRACT

Strain localization across the brittle-ductile transition is a fundamental process in accommodating tectonic movement in the mid-crust. The tectonically active Cordillera Blanca shear zone (CBSZ), a ~200-km-long normal-sense shear zone situated within the footwall of a discrete syn-convergent extensional fault in the Peruvian Andes, is an excellent field laboratory to explore this transition. Field and microscopic observations indicate consistent top-down-to-the-southwest sense of shear and a sequence of tectonites ranging from undeformed granodiorite through mylonite and ultimately fault breccia along the detachment.

Using microstructural analysis, two-feldspar and Ti-in-quartz (TitaniQ) thermometry, recrystallized quartz paleopiezometry, and analysis of quartz crystallographic preferred orientations, we evaluate the deformation conditions and mechanisms in quartz and feldspar across the CBSZ. Deformation temperatures derived from asymmetric strain-induced myrmekite in a subset of tectonite samples are 410 ± 30 to 470 ± 36 °C, consistent with TitaniQ temperatures of 450 ± 60 to 490 ± 33 °C and temperatures >400 °C estimated from microstructural criteria. Brittle fabrics overprint ductile fabrics within ~150 m of the detachment that indicate that deformation continued to lower-temperature (~280–400 °C) and/or higher-strain-rate conditions prior to the onset of pervasive brittle deformation. Initial deformation occurred via high-temperature fracturing and dissolution-precipitation in feldspar. Continued subsolidus deformation resulted in either layering of mylonites into monophase quartz and fine-grained polyphase domains oriented subparallel to macroscopic foliation or the interconnection of recrystallized quartz networks oriented obliquely to macroscopic foliation. The transition to quartz-controlled rheology occurred at temperatures near ~500 °C and at a differential stress of ~16.5 MPa. Deformation within the CBSZ occurred predominantly above ~400 °C and at stresses up to ~71.4 MPa prior to the onset of brittle deformation.

INTRODUCTION

One of the most important long-standing problems in tectonics is the localization of strain during the transition from ductile to brittle deformation in the lithosphere (Kirby, 1983; Carter and Tsenn, 1987; Rutter et al., 2001; Platt and Behr, 2011a; Sullivan et al., 2013; Spruzeniece and Piazolo, 2015). Deformation mechanisms and the relative roles of temperature, strain rate, and fluids in localizing strain can vary widely along the brittle-ductile transition (BDT). Crustal-scale shear zones are ideal settings for quantifying deformation conditions and discerning the mechanisms facilitating strain localization along the BDT. However, many such examples have protracted and complicated histories, making it difficult to discriminate the relative timing of ductile and brittle behavior (Singleton and Mosher, 2012; Cooper et al., 2017). As crustal strength along the BDT is contingent upon lithology and tectonic regime (Sibson, 1983; Carter and Tsenn, 1987), it is important to describe naturally occurring deformation in a range of geologic environments. Although previous work on crustal-scale shear zones near the BDT in granitoids is extensive (Simpson, 1985; Fitz Gerald and Stünitz, 1993; Stünitz and Fitz Gerald, 1993; Tsurumi et al., 2002; Ree et al., 2005; Pennacchioni et al., 2006; Behr and Platt, 2011; Zibra et al., 2012; Singleton and Mosher, 2012; Wintsch and Yeh, 2013; Sullivan et al., 2013; Columbu et al., 2015; Spruzeniece and Piazolo, 2015; Wehrens et al., 2016), studies of young and/or currently active extensional shear zones are less common (Bessiere et al., 2018).

Rock strength along the BDT can be affected by variables that influence brittle deformation, including fluid pressure, strain rate, effective pressure, and mineralization along failure surfaces (Byerlee, 1978; Brace and Kohlstedt, 1980; Carter and Tsenn, 1987), and those that influence ductile deformation, such as temperature, activity of water (Kirby, 1980; Tullis and Yund, 1980; Yund and Tullis, 1980), interconnectedness of minerals (Wintsch and Yeh, 2013), differential stress, lithology, deformation mechanism, and preferred mineral orientations (Rutter, 1986; Carter and Tsenn, 1987; Behr and Platt, 2011; Platt and Behr, 2011b; Cooper et al., 2017). Experimental studies have constrained many of these factors (Tullis and Yund, 1991, 1987, 1980; Hirth and Tullis, 1992, 1994; Heilbronner and Tullis, 2006; Stünitz and Tullis, 2001; Holyoke and Tullis, 2006; Holyoke and Kronenberg, 2010; Stipp and Tullis, 2003), providing a framework for studying "natural laboratories" (e.g., Lloyd et al., 1992; Hirth et al., 2001; Stipp et al., 2002a, 2002b; Wells et al., 2005; Behr and Platt, 2011, 2014; Gottardi and Teyssier, 2013; Sullivan et al., 2013; Spruzeniece and Piazolo, 2015; Viegas et al., 2016; Rahl and Skemer, 2016).

The tectonically active Cordillera Blanca shear zone (CBSZ), an ~200-km-long normal-sense shear zone in the Peruvian Andes, occurs almost entirely in the granodioritic Cordillera Blanca batholith (Atherton and Sanderson, 1987; Petford and Atherton, 1992; McNulty et al., 1998), which was emplaced at

14–5 Ma (U-Pb zircon; Mukasa, 1984; McNulty et al., 1998; Giovanni, 2007). This granodioritic intrusion is the predominant lithology in the exhumed footwall of the Cordillera Blanca detachment normal fault, which is the expression of the upper, brittle portion of the CBSZ and has been active since ca. 5 Ma (Bonnot, 1984; Giovanni, 2007). Tectonic fabrics progress from undeformed granodiorite in the core of the batholith in the east, through mylonites and ultramylonites toward the west, culminating in cataclasite and breccia along the detachment surface. The CBSZ is an excellent case study of the BDT, as the relatively simple deformation history and consistent lithology facilitate comparison of fabrics, deformation mechanisms, and deformation conditions at different structural levels across the BDT.

We present new data characterizing mid-crustal deformation within the CBSZ including deformation temperatures of quartz and feldspar, quartz crystallographic preferred orientations (CPOs), flow stress, and microstructural relationships relating to changing deformation mechanisms. Previous work describes the transition from magmatic to subsolidus tectonic fabrics in the CBSZ (Petford and Atherton, 1992), but no constraints on ductile deformation conditions are presently available. An additional motivation for this study is to offer the first quantitative constraints on ductile to brittle deformation conditions within the CBSZ and evaluate the deformation mechanisms that facilitate the fabric transition described by Petford and Atherton (1992). In this study, we present data supporting early deformation by high-temperature fracturing in a feldspar-controlled framework followed by predominantly quartz-controlled rheology, with at least local polyphase-controlled rheology within layered mylonites. Our results indicate that deformation during exhumation produced overprinting fabrics reflecting changes in deformation mechanisms and an increase in strain rate. Strain localized from an ~450 m thick plastic shear zone to an ~150 m thick brittle fault zone along a discrete detachment fault.

GEOLOGIC BACKGROUND AND SAMPLE DESCRIPTIONS

Subduction along the Andean margin of South America began by at least the Jurassic and cycled between steep– and shallow–to–flat slab subduction until its present configuration (James, 1971; Jordan et al., 1983; Ramos, 1999). The Cordillera Blanca range is situated above the Peruvian flat-slab segment of the present margin (Gutscher et al., 1999; McNulty and Farber, 2002), within the central-eastern Cordillera Occidental along the western margin of the Marañón fold-and-thrust belt (Fig. 1). West of the Cordillera Blanca lies the Cordillera Negra, a 54–15 Ma volcanic arc related to normal subduction along the Peru-Chile trench (Petford and Atherton, 1992; Scherrenberg et al., 2014, 2016). Beginning at ca. 15 Ma, magmatism migrated eastward, culminating in the intrusion and crystallization of the Cordillera Blanca batholith from 13.7 ± 0.3 Ma to 5.3 ± 0.3 Ma (U-Pb zircon; Mukasa, 1984; Giovanni, 2007) and eruption of the associated Yungay and Fortaleza ignimbrites between 8.7 ± 1.6 and 4.5 ± 0.2 Ma ($^{40}Ar/^{39}Ar$ biotite; Bonnot, 1984; Giovanni et al., 2010) and between 6.2 ± 0.2 and 4.9 ± 0.2 Ma, respectively (K-Ar biotite; Wilson, 1975; Cobbing et al., 1981). These events mark the last episode of arc magmatism in this region (Cobbing et al., 1981; Bonnot, 1984; Mukasa, 1984; Petford and Atherton, 1996; McNulty et al., 1998; McNulty and Farber, 2002; Giovanni, 2007; Giovanni et al., 2010). Crustal shortening associated with convergence of the South American and Nazca plates also migrated inboard, east of the Marañón massif, to the present Subandean fold-and-thrust belt (Fig. 1).

The Cordillera Blanca range is cored by the granodiorite-leucogranodiorite Cordillera Blanca batholith (Atherton and Sanderson, 1987; Petford and Atherton, 1992). Batholith emplacement is estimated at ~300 MPa (McNulty and Farber, 2002) and >200 MPa (Petford and Atherton, 1992) from mineral assemblages in the pelitic contact aureole, and at 90 ± 10 MPa to 260 ± 30

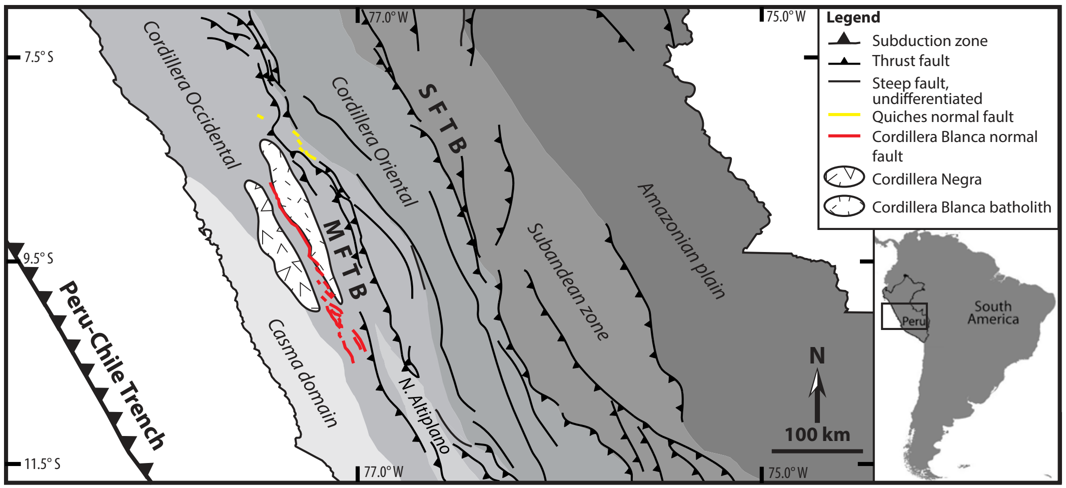

Figure 1. Tectono-physiographic map of central Peru, after Pfiffner and Gonzalez (2013). MFTB—Marañón fold-and-thrust belt; SFTB—Subandean fold-and-thrust belt. Inset shows location of tectono-physiographic map with respect to South American continent.

MPa at 720–800 °C from recent amphibole thermobarometry of batholith rocks (Margirier et al., 2016). The batholith cooled rapidly at 200 °C/m.y. until ca. 4 Ma and subsequently cooled at 25 °C/m.y. from 4 to 0 Ma (Margirier et al., 2015). Extension along the Cordillera Blanca detachment initiated at ca. 5 Ma (Bonnot, 1984; Giovanni, 2007), accommodating 12–15 km of normal-sense displacement (Giovanni et al., 2010). A series of glacially and fluvially incised ravines (quebradas) cut across the Cordillera Blanca nearly orthogonal to strike of the range (Wise and Noble, 2003), providing exposure of the full ductile-to-brittle fabric gradient developed in the CBSZ (Fig. 2). Fault scarps along the detachment truncate glacial moraines, offsetting moraine crests by ~2–70 m (Bonnot et al., 1988; Schwartz, 1988; Siame et al., 2006). The most recent faulting is bracketed by detrital charcoal in colluvium between 2440 ± 1060 and 750 ± 80 ^{14}C yr B.P, and by positioning of pre-Incan structures relative to fault scarps at 1500–2000 yr B.P. (Schwartz, 1988). The hanging wall comprises Jurassic to Cretaceous sediments, Eocene–Pliocene volcanics, and Miocene–Pliocene sediments of the Lloclla Formation (Cobbing et al., 1981; Petford and Atherton, 1992; Giovanni et al., 2010; Margirier et al., 2015). Hot springs issue along the main detachment system and along steeply dipping faults and inferred synthetic faults proximal to the shear zone (Newell et al., 2015).

We present data from samples collected in Quebrada Gatay (Fig. 2) and describe CBSZ deformation relative to structural depths below the exposed detachment surface. Quebrada Gatay samples (Table S1 in the Supplemental Files[1]) were collected across the ductile-to-brittle fabric transition and are mostly leucogranodiorite, with a small number from quartz veins oriented parallel to foliation and phyllites presumably from a lens of the Jurassic Chicama Formation host rock. Supplemental information is available in Tables S1–S2, Figures S1–S2, and Text S1–S3 (footnote 1).

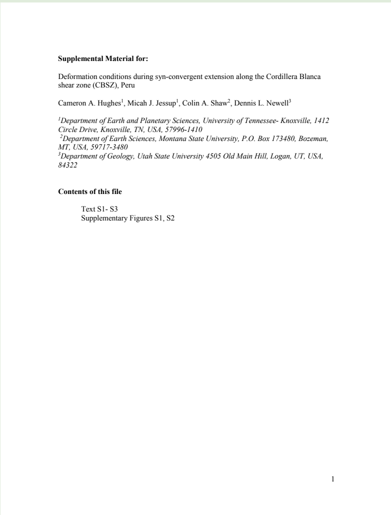
Supplemental Material for:

Deformation conditions during syn-convergent extension along the Cordillera Blanca shear zone (CBSZ), Peru

Cameron A. Hughes[1], Micah J. Jessup[1], Colin A. Shaw[2], Dennis L. Newell[3]

[1]Department of Earth and Planetary Sciences, University of Tennessee- Knoxville, 1412 Circle Drive, Knoxville, TN, USA, 57996-1410
[2]Department of Earth Sciences, Montana State University, P.O. Box 173480, Bozeman, MT, USA, 59717-3480
[3]Department of Geology, Utah State University 4505 Old Main Hill, Logan, UT, USA, 84322

Contents of this file

Text S1- S3
Supplementary Figures S1, S2

1

[1]Supplemental Files. Table S1: Sample locations. Table S2: Mineral chemistry used for two-feldspar thermometry. Text S1: Cathodoluminescence and Titanium-in-Quartz (TitaniQ) electron probe microanalyzer methods. Text S2: Raw data processing methods for electron backscatter diffraction (EBSD) analyses. Text S3: Discussion of TitaniQ reliability for this study. Figure S1: Recrystallized quartz grain size distributions. Figure S2: EBSD-derived evidence for grain boundary sliding. Please visit https://doi.org/10.1130/GES02040.S1 or access the full-text article on www.gsapubs.org to view the Supplemental Files.

METHODS

Thirty-two (32) samples were collected from Quebrada Gatay in July 2013 and were cut into thin sections perpendicular to foliation and parallel to lineation (*X-Z* sections). We used optical petrography, electron backscatter diffraction (EBSD) analysis, and electron probe microanalyzer (EPMA) analysis to evaluate microstructures, quartz CPOs, deformation temperature, and flow stress across the fabric progression from undeformed granite to ultramylonite and cataclasite.

Deformation Temperatures

Two-Feldspar Geothermometry

Deformation temperatures were estimated for samples with asymmetric strain-induced myrmekite (ASIM) using two-feldspar thermometry of coexisting feldspars within the symplectite (Simpson and Wintsch, 1989; Langille et al., 2010). ASIM develops when aqueous Na^+ is concentrated at high-stress sites along K-feldspar grain boundaries (Fig. 3A; Simpson and Wintsch, 1989). High strain facilitates the reaction (Simpson and Wintsch, 1989; Tsurumi et al., 2002; Menegon et al., 2008):

$$\text{K-feldspar} + Na^+ \rightarrow \text{Na-feldspar} + \text{quartz} + K^+. \quad (1)$$

The resulting ASIM microstructure comprises a K-feldspar porphyroclast impinged by asymmetrically distributed albite-oligoclase lobes that grow parallel to the maximum incremental shortening axis and contain vermicular quartz. K-feldspar recrystallizes as tails in low-strain sites (Fig. 3A; Simpson and Wintsch, 1989).

We derive ASIM deformation temperatures using chemical compositions from along the interface of the K-feldspar porphyroclast and the Na-feldspar myrmekitic lobe (Fig. 3B; Langille et al., 2010). Mineral compositions were obtained using the Cameca SX-100 EPMA at the University of Tennessee–Knoxville (UTK; Knoxville, Tennessee, USA) by spot analysis at 15 keV, 10 nA, 5 µm spot size, and 30 s counting time. X-ray maps (Na, K, Si, and Fe) were made at 15 keV, 20 nA, 50 ms dwell time, and 1 µm spot size to evaluate compositional zoning in porphyroclasts and myrmekite lobes and to characterize matrix phases. Multiple lobes from individual ASIM-bearing porphyroclasts were analyzed to determine the average deformation temperature. Temperatures were calculated using the two-feldspar thermometer (Stormer, 1975; Whitney and Stormer, 1977):

$$T(\mathrm{K}) = \frac{\left\{7973.1 - 16{,}910.6X_{ab,\,AF} + 9901.9X^2_{ab,\,AF} + \left(0.11 - 0.22X_{ab,\,AF} + 0.11X^2_{ab,\,AF}\right)(10P)\right\}}{\left\{-1.9872\ln\left(\dfrac{X_{ab,\,AF}}{\alpha_{ab,\,PL}}\right) + 6.48 - 21.58X_{ab,\,AF} + 23.72X^2_{ab,\,AF} - 8.62X^3_{ab,\,AF}\right\}}, \quad (2)$$

where $X_{ab,AF}$ is normalized molar concentration of albite in alkali feldspar, P is pressure (MPa), and $\alpha_{ab,PL}$ is the activity of albite in plagioclase. Because shear sense from ASIM is consistent with shear sense from other indicators, temperatures derived from ASIM are assumed to be deformation temperatures (Simpson and Wintsch, 1989; Langille et al., 2010). Temperatures were calculated at 100 MPa and 300 MPa pressures and are presented here calculated at 300 MPa with errors of the 2σ standard deviation of feldspar compositions propagated through the thermometer. Reported temperatures and errors do not include the ±50 °C error from the thermometer. Mineral compositions used for thermometry calculations are reported in Table S2 (footnote 1).

Titanium-in-Quartz (TitaniQ) Geothermometry

Titanium-in-quartz (TitaniQ) thermometry utilizes the log-linear relationship between increasing Ti concentration in quartz with increasing temperature (Wark and Watson, 2006). Established as a reliable thermometer in igneous and volcanic systems when pressure and Ti activity (α_{TiO_2}) are constrained, TitaniQ has also been increasingly used in greenschist facies shear zones to determine

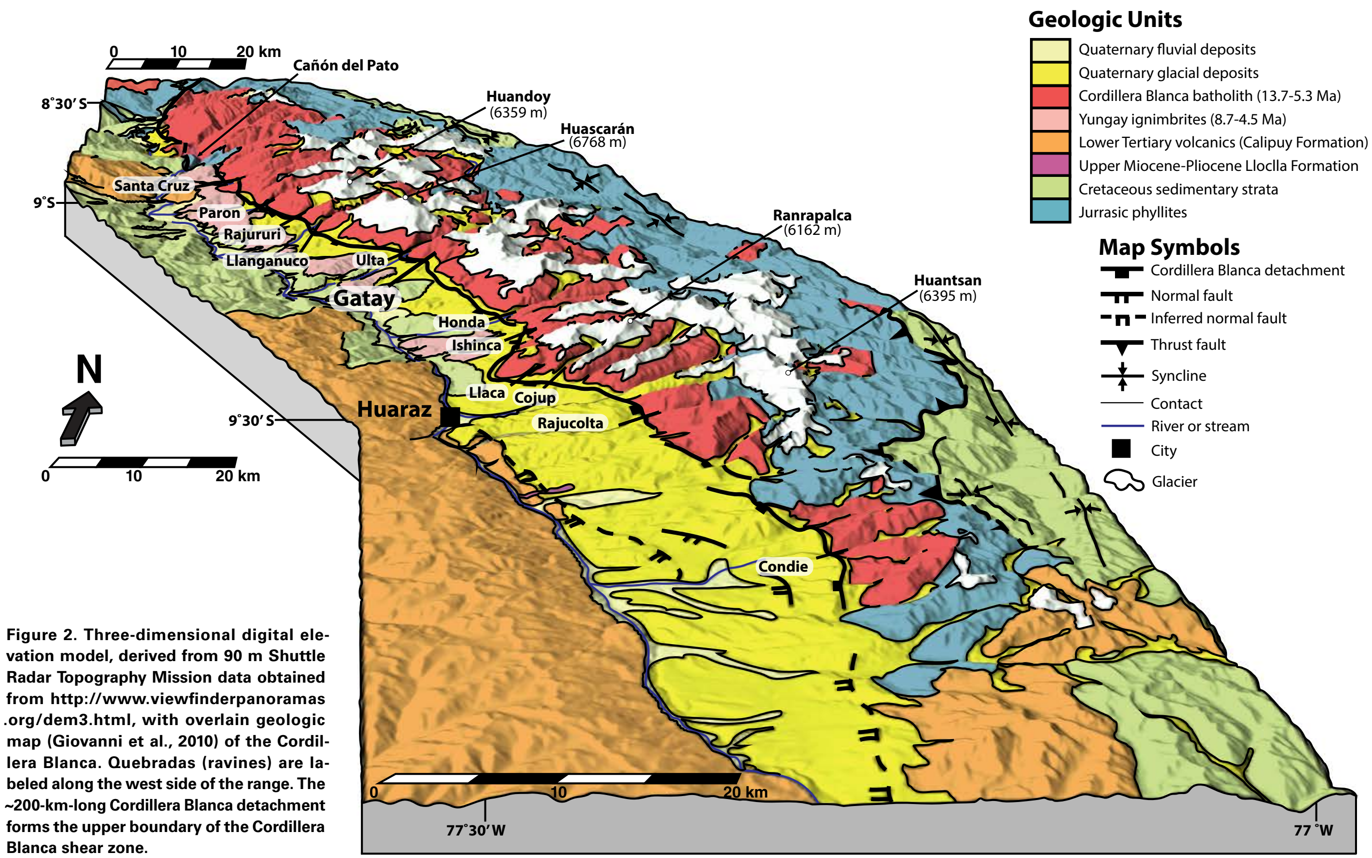

Figure 2. Three-dimensional digital elevation model, derived from 90 m Shuttle Radar Topography Mission data obtained from http://www.viewfinderpanoramas.org/dem3.html, with overlain geologic map (Giovanni et al., 2010) of the Cordillera Blanca. Quebradas (ravines) are labeled along the west side of the range. The ~200-km-long Cordillera Blanca detachment forms the upper boundary of the Cordillera Blanca shear zone.

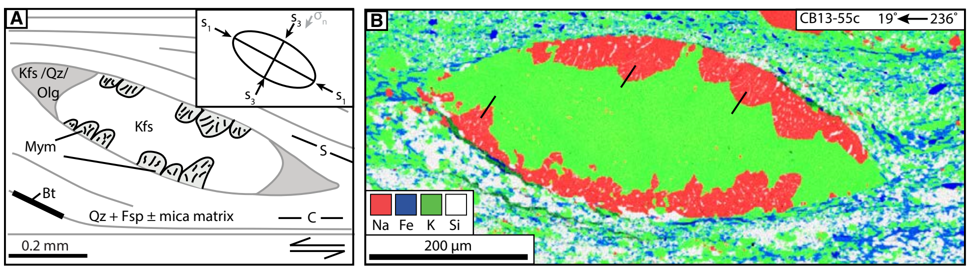

Figure 3. (A) Schematic diagram of strain-induced myrmekite (after Simpson and Wintsch, 1989). Inset shows the principal strain ellipse. Orientation of normal stress (σ_n) relative to myrmekite from Simpson and Wintsch (1989). Bt—biotite; Kfs—potassium feldspar; Mym—myrmekite; Fsp—feldspar; Olg—oligoclase (red); Qz—quartz. Albite-oligoclase myrmekite lobes grow toward the center of the host porphyroclast. Lobes are concentrated at high-strain sites, shown relative to S-C mylonitic fabric. (B) X-ray compositional map of major element compositions of asymmetric strain-induced myrmekite microstructure. Surrounding matrix is recrystallized quartz (white), biotite (blue), and K-feldspar (green). Black lines denote locations of spot analysis transects for use in thermometry calculations. Arrow notation indicates trend and plunge of lineation, with arrow pointing down-plunge.

deformation conditions (e.g., Kidder et al., 2013). Some debate occurs regarding the reliability of TitaniQ in different dynamic recrystallization regimes, though there is general agreement that TitaniQ is reliable under conditions required for grain-boundary migration (GBM) recrystallization (Thomas et al., 2010; Behr et al., 2011; Grujic et al., 2011; Thomas and Watson, 2012; Kidder et al., 2013; Nachlas et al., 2014; Cross et al., 2015). Recent experimental evidence suggests that Ti concentrations are efficiently re-equilibrated during recrystallization by grain boundary formation and migration (Nachlas et al., 2018). Because high-temperature and/or low-strain-rate conditions tend toward preserving Ti concentrations on the order of 10–100 ppm, concentrations can be determined on an EPMA for quartz exhibiting GBM (high-temperature and/or low-strain-rate) recrystallization microstructures (Behr et al., 2011; Grujic et al., 2011; Nachlas et al., 2014, 2018). Samples without GBM recrystallization microstructures were not considered for analysis in this study due to the likelihood that Ti concentrations would be below the detection limit of the EPMA at UTK, or otherwise may be preserving inherited Ti concentrations from higher-temperature deformation (i.e., Grujic et al., 2011). Although Nachlas et al. (2018) suggested that Ti should be re-equilibrated for recrystallized quartz even at low temperatures, resolving possible inherited concentrations versus recrystallized Ti concentrations would require higher-precision instrumentation.

Cathodoluminescence (CL) imaging was conducted prior to EPMA analyses. CL imaging details and EPMA conditions for TitaniQ analyses are provided in Text S1 (footnote 1). Temperatures were calculated using the thermobarometer of Thomas et al. (2010):

$$T(^{\circ}\mathrm{C}) = \frac{60{,}952 + 1741(P/100)}{1.520 - R \times lnX_{\mathrm{TiO_2}}^{\mathrm{Qtz}} + R \times ln\alpha_{\mathrm{TiO_2}}} - 273.15, \quad (3)$$

where P is pressure (MPa), R is the gas constant, $X_{\mathrm{TiO_2}}^{\mathrm{Qtz}}$ is the concentration of Ti in quartz (ppm), and $\alpha_{\mathrm{TiO_2}}$ is the TiO_2 activity, and the thermobarometer of Huang and Audétat (2012):

$$\log\mathrm{Ti(ppm)} = -0.27943 \times \frac{10^4}{T} - 660.53 \times \left(\frac{(P/100)^{0.35}}{T}\right) + 5.6459, \quad (4)$$

where T is temperature (Kelvin) and P is pressure (MPa). TiO_2 activity for silicic igneous rocks can be difficult to constrain (Huang and Audétat, 2012), although for most igneous and metamorphic rocks, $\alpha_{\mathrm{TiO_2}}$ is above ~0.5, and in silicic melts, typically above ~0.6 (Hayden and Watson, 2007). Activity can be further constrained by presence of ilmenite or titanite ($\alpha_{\mathrm{TiO_2}}$ 0.7–0.8) (Ghent and Stout, 1984; Peterman and Grove, 2010).

Quartz Crystallographic Preferred Orientations (CPOs)

Quartz CPOs were obtained using EBSD on the field emission gun–scanning electron microscope at the Imaging and Chemical Analysis Laboratory (ICAL) at Montana State University (Bozeman, Montana, USA). Analyses were conducted at 20 Pa and 20–30 kV, and Kikuchi band diffraction patterns were collected for quartz for 75 reflectors using Oxford Instruments HKL Channel 5 Flamenco software (ver. 5.5). Step sizes ranged from 1.5 to 5 µm depending on minimum grain size observed under petrographic microscope. Pole figures of quartz *c*- and *a*-axis orientations were constructed using the MTEX toolbox (Bachmann et al., 2010) for MATLAB. Details on raw EBSD data processing are provided in Text S2 (footnote 1). EBSD was applied to eight representative samples in interconnected quartz-rich domains as far away from other phases as possible to minimize potential effects from pinning. CPO pole figures are lower-hemisphere projections of *c*- and *a*-axes using one point per grain, where grains are defined using at least eight pixels and a critical misorientation of 10°, contoured at 7.5° half-width (see Text S2 [footnote 1] for details). Fabric strength was evaluated using the M-index of Skemer et al. (2005) and the J-index of Bunge (1982).

Flow Stress

Differential stresses were estimated using recrystallized grain-size piezometry, where differential stress and recrystallized grain size are inversely related by the following expression (Twiss, 1977; Stipp and Tullis, 2003):

$$d = \beta\sigma^{m}. \quad (5)$$

Differential stresses were calculated using the piezometer calibration of Stipp and Tullis (2003), modified after Holyoke and Kronenberg (2010), where d is the root mean square (RMS) of the grain-size distribution, β is an empirically derived constant (3640 µm/MPa^{m}), σ is differential stress, and m is an experimentally derived stress exponent (–1.26). These values were compared to the recent "sliding-resolution" piezometer calibration for EBSD-derived grain sizes, where β and m are $10^{4.22 \pm 0.51}$ and –1.59 ± 0.26, respectively (Cross et al., 2017b). Grain-size distributions (Fig. S1 [footnote 1]) were derived from EBSD analysis on representative quartz-rich domains from mylonitic granodiorite and mylonitic quartz veins, where grain size was defined as the diameter of an equivalent-area circle. Errors on differential stress estimates are the standard deviation relative to RMS for the grain-size distribution propagated through the piezometer.

RESULTS

Mesoscale Observations

Mean foliation from Quebrada Gatay strikes 167°± 5° and dips 23° ± 5°, and mean stretching lineation trends toward 239° ± 6°, plunging 24° ± 6° (Fig. 4A). The detachment surface exposed at Quebrada Gatay (Fig. 4A) strikes ~150° and dips ~26° based on a series of three-point problems solved using Google Earth. Data from structural positions between 150 and 300 m below the detachment are sparse due to steep terrain and vegetative cover. An injection complex of leucogranodiorite veins intrudes into a host rock (shale) lens 130–150 m below

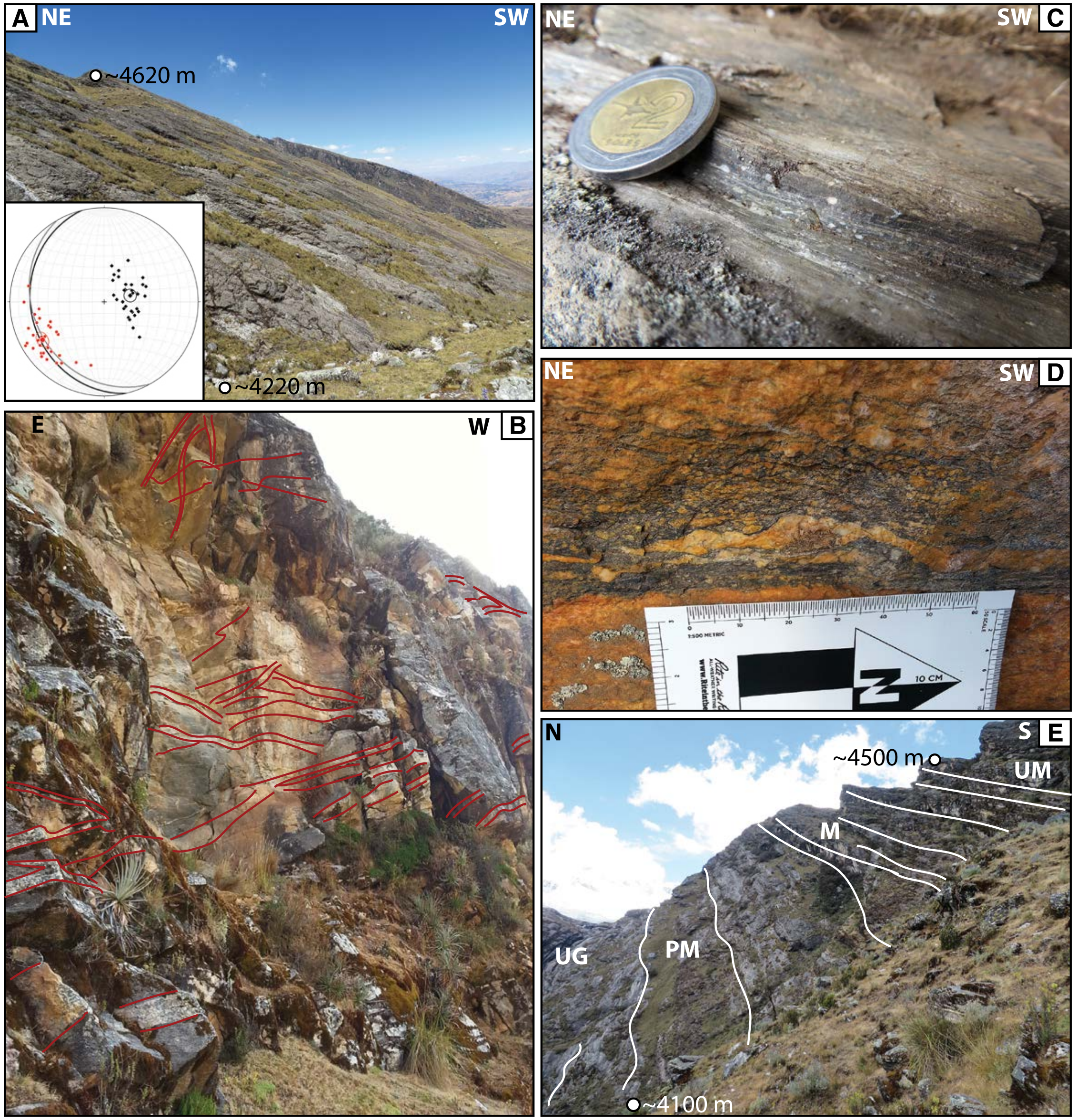

Figure 4. Field photos from the south side of Quebrada Gatay. (A) Detachment surface looking to the southeast. Inset: stereonet of poles to foliation (black diamonds, $N = 33$), mean foliation plane (black great circle), stretching lineations (red circles, $N = 33$), and mean detachment surface derived from Google Earth (gray great circle). Large symbols are Fisher mean vectors with 95% confidence intervals. (B) Injection complex of leucogranitic veins into a lens of Jurassic Chicama Formation shale. Outcrop in view is ~8 m tall. (C) Ultramylonitic foliation with feldspar sigma clasts indicating dextral (top-to-the-southwest) shear and asymmetric folding. Peruvian two-sol piece (~2.4 cm diameter) for scale. (D) Biotite-rich domain above a foliation-parallel quartz vein. (E) Pervasive southwest-dipping foliation across the Cordillera Blanca shear zone. White circles mark elevation. UG—undeformed granite; PM—protomylonite; M—mylonite; UM—ultramylonite.

the detachment surface (Fig. 4B). Localized zones of mylonite to ultramylonite from 5 to 50 cm thick occur at structural positions as deep as 385 m below the detachment within otherwise undeformed to protomylonitic granite (Fig. 4C). Quartz veins 10–60 cm thick occur parallel and subparallel to foliation throughout the shear zone (Fig. 4D). A progression in fabric from undeformed granodiorite to ultramylonite with consistent SSW-dipping foliation is observed (Fig. 4E) and is the basis for interpretations of deformation mechanisms and conditions during shear zone evolution.

Microstructural Observations

Observed microstructures can be divided based on interconnected phases into feldspar, quartz, mica, and polyphase domains. These domains are spatially variable such that the rheological framework may be controlled by either quartz, feldspar, mica, or a combination thereof.

Feldspar

Within ~150 m of the detachment, throughgoing features such as fractures, microfaults, and cataclasite cut across feldspar and adjacent phases (Fig. 5A, Table 1). At structurally high positions, feldspar porphyroclasts are commonly fractured and filled with quartz and/or K-feldspar. These fractures tend to be isolated to feldspar porphyroclasts and do not extend into surrounding phases. Some feldspar fragments are rotated with respect to the other fragment(s) within the original porphyroclast, forming V-shaped pull-apart structures (Fig. 5B; i.e., Fukuda et al., 2012; Hippertt, 1993; Samanta et al., 2002). Undulose extinction and deformation lamellae are common within plagioclase porphyroclasts.

Fine-grained feldspar aggregates occur in layered mylonitic to ultramylonitic samples at structural depths from 430 to 111 m. Finely recrystallized grains mantle porphyroclasts and form tails on σ- and δ-type feldspar porphyroclasts that deflect into quartz + feldspar shear bands (Fig. 5C). Within these samples, myrmekite commonly has formed along high-strain sites of K-feldspar porphyroclasts as well as within fine-grained plagioclase–K-feldspar aggregates (Fig. 5D).

Interconnected networks of feldspar porphyroclasts or phenocrysts occur below 350 m. At 350 m, mylonitic samples contain interconnected plagioclase phenocrysts that exhibit bulging recrystallization at feldspar-feldspar grain boundaries (Fig. 5E) and contain biotite at triple junctions (Fig. 5F). Biotite also occurs in low-strain sites of boudinaged plagioclase where interconnected quartz and interconnected feldspar coincide. Plagioclase boudins are relatively symmetrical, are tapered yet connected, and have concave-faced boundaries (Fig. 5G). Weakly deformed samples at the deepest structural positions are characterized by interconnected networks of K-feldspar and plagioclase phenocrysts that exhibit intragranular fractures (Figs. 5H, 5I). Recrystallization has occurred along plagioclase grain boundaries and along intragranular fractures within plagioclase and K-feldspar phenocrysts (Fig. 5I). Large (~500 μm) myrmekite lobes have grown into K-feldspar phenocrysts (Fig. 5J).

Quartz

Quartz domains occur primarily either as interconnected networks surrounding other phases or as monophase aggregates in layered mylonites. Quartz commonly displays grain-shape fabrics that define S-planes and exhibits dynamic recrystallization microstructures spanning the range of characteristic grain-boundary microstructures described by Stipp et al. (2002a, 2002b; Fig. 6). Distribution with respect to structural depth of quartz recrystallization microstructures, along with that of feldspar microstructures discussed above and microfabrics including interconnected phase, inferred quartz crystallographic slip systems, and deformation temperatures discussed in the following sections, are summarized in Figure 7.

In the upper ~150 m of the shear zone, ductile fabrics including bulging (BLG) and subgrain rotation (SGR) recrystallization microstructures in quartz are overprinted by brittle fabrics (Figs. 6A–6D; Table 1). Serrated grain boundaries and fine recrystallized grains characteristic of BLG recrystallization (Stipp et al., 2002b) occur in samples that also contain polygonal subgrains and new rotated grains within quartz porphyroclasts, characteristic of SGR recrystallization (Stipp et al., 2002a; Fig. 6E). Samples within the upper ~150 m of the shear zone that exhibit only ductile fabrics contain microstructures indicative of SGR recrystallization or a combination of BLG and SGR.

Samples from deeper than ~150 m below the detachment preserve ductile deformation in quartz and lack evidence for throughgoing brittle deformation. Quartz in most samples at these positions exhibits dominant SGR recrystallization microstructures, large grains with amoeboidal grain boundaries and commonly undulose extinction indicative of grain boundary migration (GBM) recrystallization (Stipp et al., 2002a), or both SGR and GBM recrystallization microstructures (Figs. 6F–6J). Two samples from 384 to 386 m below the detachment record a combination of BLG and SGR recrystallization in quartz (Fig. 6I).

At structurally deep positions, quartz forms discontinuous lenses and/or fills fractures in feldspar phenocrysts (Figs. 5H, 6J, 6K). Structurally deepest positions preserve large amoeboid quartz grains characteristic of GBM recrystallization microstructures within isolated quartz pockets at the interstices between feldspar phenocrysts (430 m; Fig. 5H). Planar, orthogonal subgrain boundaries indicative of chessboard extinction in quartz occur at deepest structural positions (446 m; Figs. 5H, 6K).

Microfabrics

Microfabrics described here refer to the interconnected phase(s) present as well as which phases define S-, C-, and C′-surfaces and which of these surfaces is prominent within the foliation.

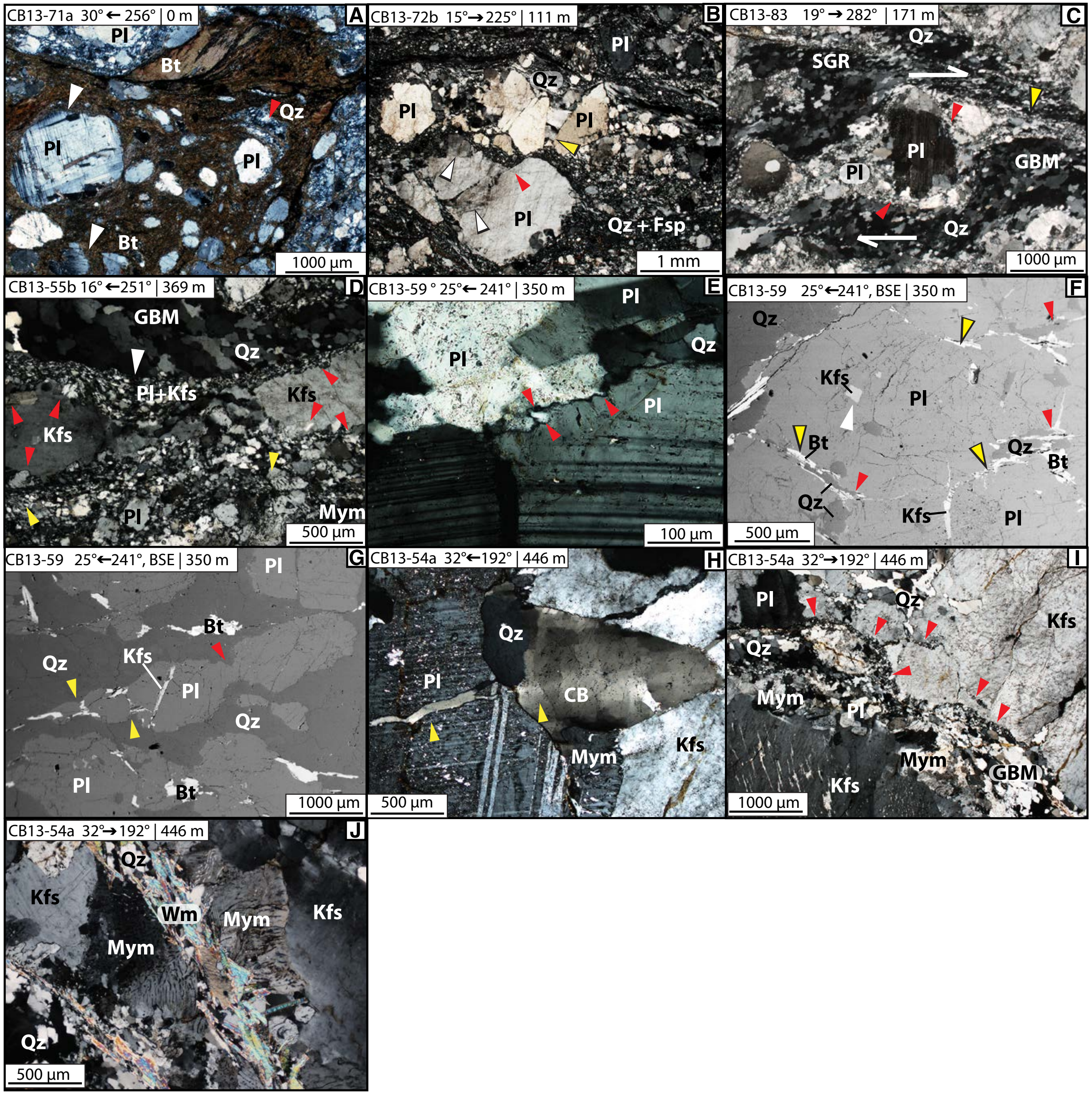

Figure 5. Representative images of feldspar microstructures. Images are cross-polarized light (XPL) photomicrographs unless otherwise noted. Labels denote trend and plunge of lineation, with arrow pointing down-plunge, and structural depth below the Cordillera Blanca detachment (in meters); arrowhead indicators are specified below as (color). Bt—biotite; Fsp—feldspar (undifferentiated); Kfs—K-feldspar; Mym—myrmekite; Pl—plagioclase; Qz—quartz; Wm—white mica. (A) Cataclasite including internally deformed plagioclase clasts (white) and dynamically recrystallized quartz (red) in biotite-rich (left) and biotite-poor (right) quartz-feldspar matrix. (B) Fractured plagioclase phenocrysts with small offset (red) and V-pull-apart structure with quartz infill (yellow). Patchy extinction is present near the offset fracture (white). (C) Dynamically recrystallized plagioclase (red), creating a core-mantle structure. Recrystallized feldspar tail deflects into a quartz-rich shear band; grain size of quartz and plagioclase decreases with deflection into the shear band (yellow). Subgrain rotation (SGR) and grain-boundary migration (GBM) recrystallization microstructures are present in the adjacent quartz domain. (D) Interconnected domain of recrystallized plagioclase and K-feldspar (white) adjacent to quartz domain exhibiting GBM recrystallization microstructure. K-feldspar porphyroclasts contain recrystallized tails and asymmetric strain-induced myrmekite (red). Myrmekite is also present in recrystallized plagioclase + K-feldspar matrix (yellow). (E) New grains formed by bulging recrystallization in plagioclase (red). (F) Backscattered electron (BSE) image of interconnected plagioclase domain, biotite, and quartz along triple junctions (red). Biotite occupies grain boundaries between plagioclase phenocrysts (yellow). K-feldspar is hosted as inclusions within phenocrysts and as fracture fill (white). (G) BSE image of boudinaged plagioclase within quartz matrix (red). Biotite and quartz occupy dilatant sites in pinch-and-swell structure (yellow). (H) Wedge-shaped K-feldspar fracture filled with quartz exhibiting chessboard extinction (CB) that is continuous crystallographically with quartz within a plagioclase fracture (yellow). Image is rotated 90° counterclockwise from *X-Z* orientation. (I) Recrystallized plagioclase along K-feldspar grain boundaries and fractures (red). GBM recrystallization microstructure is present in interstitial quartz. (J) Myrmekite growth into K-feldspar, with white mica along the initial K-feldspar grain boundary.

TABLE 1. MICROSTRUCTURAL OBSERVATIONS WITH RESPECT TO STRUCTURAL DEPTH FOR ALL QUEBRADA GATAY SAMPLES, CORDILLERA BLANCA SHEAR ZONE

Sample	Rock type*	Fabric†	Structural depth (m)	Microstructures§		Rheological domain#
				Quartz	Feldspar	
CB13-71a	gd	cat	0	BLG, SGR	P, FR, D	D^{X}
CB13-71b	gd	cat	0	BLG, SGR	P, D, FR	D^{X}
CB13-77a	gd	myl	92	BLG, SGR	D, B, FR	C, D
CB13-77b	p	sch	93	BLG, SGR, U	T, DRX	–**
CB13-77c	qv	umyl	94	SGR	P, FR, T	D^{X}
CB13-72a	gd	myl	111	SGR, BLG	M, ASIM, E, FR, D, P	C, D, E, F
CB13-72b	gd	myl	111	BLG, SGR	P, T, PA, FR, F	C, D, F
CB13-73a	gd	cat	126	BLG, SGR	T	D^{X}
CB13-73b	gd	cat	126	BLG. SGR, PT	PT	D, E^{X}
CB13-74a	gd	cat	131	SGR, BLG	D, P	D^{X}
CB13-74b	p	sch	131	GBM, SGR	D, P, T, BD, K	–
CB13-81	p	sch	131	GBM	T, DRX	–
CB13-82	gd	myl	131	SGR, GBM	ASIM, P, T, DRX, PA, D, K	D, E, F
CB13-79	gd	pmyl	134	GBM, SGR	DRX, ASIM	C, D, F
CB13-80a	gd	umyl	134	SGR	N.A.††	E
CB13-80b	p	sch	134	GBM, SGR	N.A.	–
CB13-75	gd	myl, br	146	BLG, SGR	ASIM, D, P, B, K, PA, FR	D, F^{X}
CB13-76	gd	myl	149	SGR, BLG	D, T, PA	D^{X}
CB13-78	gd	myl	152	BLG, SGR	ASIM, D, P, T, PA, FR	C, D, F
CB13-83	gd	myl	171	SGR, GBM	ASIM, D, U, DRX, T, FR	C, F
CB13-84	gd	myl	232	GBM	ASIM, F, U, DRX, FR	C, E, F
CB13-53	gd	myl	304	GBM	M, DRX, ASIM, F	F
CB13-85	gd	myl	312	SGR	ASIM, D, DRX, M, F, FR	C, F
CB13-59	gd	myl	350	GBM	BD, BLG	B
CB13-58	gd	myl	354	SGR, GBM	M	F
CB13-55b	gd	pmyl	369	GBM	M, ASIM, U, BLG	C, F, E
CB13-55c	gd	umyl	369	SGR	ASIM, U, DRX, PA, T	C, G
CB13-57a	gd	myl	384	BLG, SGR	DRX, T, PA	D, E, F, G
CB13-57b	qv	umyl	385	BLG	N.A.	D
CB13-57c	qv	umyl	386	SGR, BLG	N.A.	D
CB13-56	p	sch	390	GBM	T	–
CB13-55a	gd	pmyl	430	GBM, SGR	BLG, M, FR, ASIM, U	A, F
CB13-54a	gd	wd	446	CB, GBM	BLG, M, FR	A

Note: Summary table of sample descriptions, results, and interpreted rheological domains.

*gd—granodiorite; p—pelite; qv—quartz vein.

†br—breccia, cat—cataclasite, myl—mylonite, pmyl—protomylonite; sch—schist; umyl—ultramylonite, wd—weakly deformed.

§ASIM—asymmetric strain-induced myrmekite; B—bookshelf feldspar; BD—boudinage; BLG—bulging recrystallization; CB—chessboard extinction; D—deformation lamellae; DRX—dynamic recrystallization; E—exsolution; F—flame perthite; FR—fractured; GBM—grain-boundary migration recrystallization; K—kinked; M—myrmekite (non–strain induced); P—patchy extinction; PA—pull-aparts; PT—pseudotachylyte; SGR—subgrain rotation recrystallization; T—feldspar tails; U—undulose extinction.

#Rheological domains A–F from Figure 11 for granodiorite and quartz veins prior to throughgoing brittle overprinting, which is denoted by X.

**–, not applicable (pelite lithology)

††N.A.: not applicable (no feldspar present)

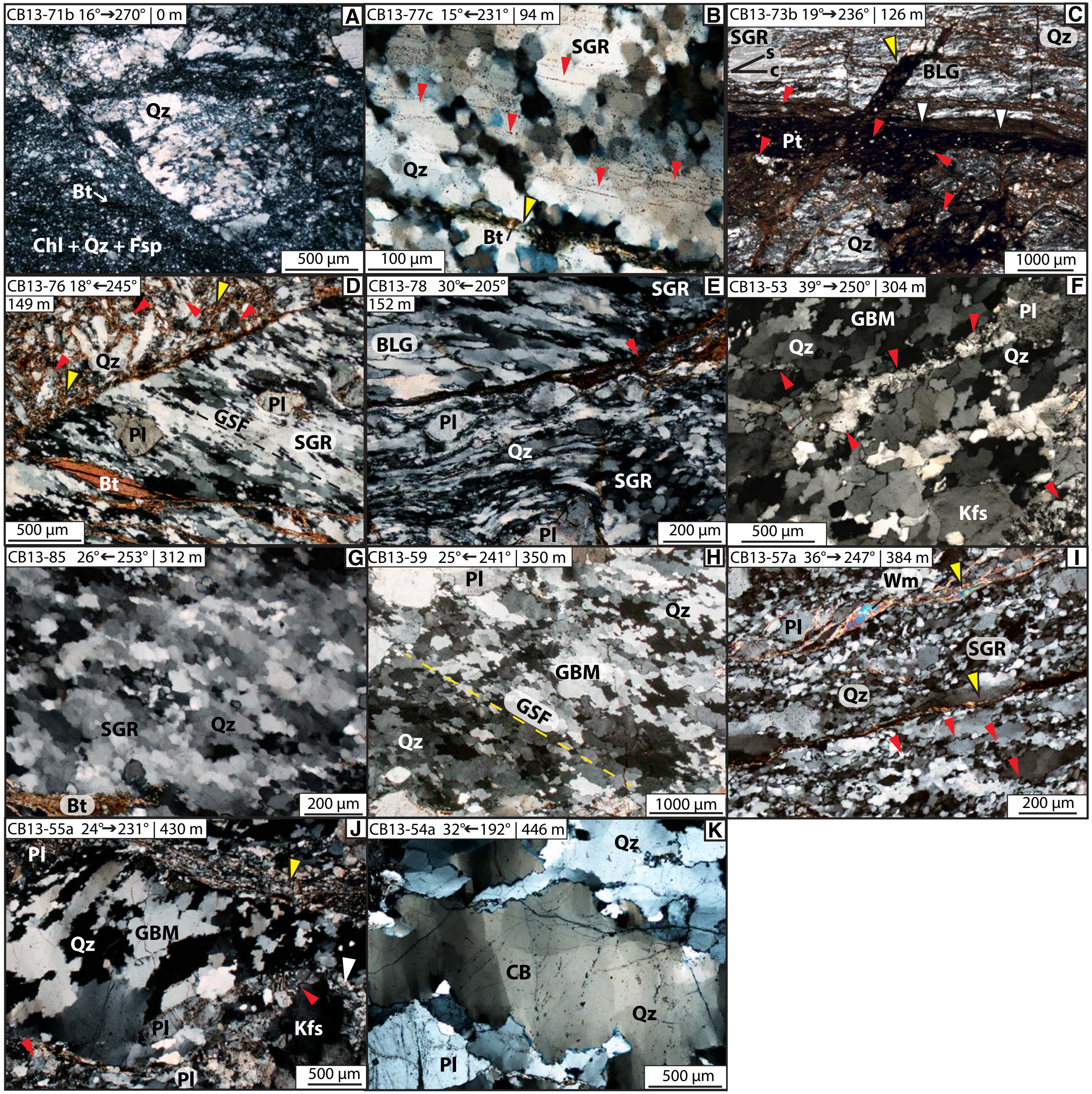

Figure 6. Cross-polarized light photomicrographs of quartz microstructures. Labels denote trend and plunge of lineation, with arrow pointing down-plunge and structural depth below the Cordillera Blanca detachment (in meters); arrowhead indicators are specified below as (color). Bt—biotite; Chl—chlorite; Fsp—feldspar (undifferentiated); Kfs—K-feldspar; Pl—plagioclase; Qz—quartz; Wm—white mica. Quartz recrystallization microstructures: BLG—bulging; SGR—subgrain rotation; GBM—grain boundary migration. (A) Microfaults truncating mylonitic foliation at high angles. Mylonitic fabric records SGR and BLG recrystallization in quartz. (B) Quartz SGR overprinted by fluid inclusion planes (red) oriented subparallel to shear bands (yellow). (C) Pseudotachylyte injection vein (yellow) and pseudotachylyte layer oriented parallel to mylonitic foliation (white), containing deformed mylonitic clasts and plagioclase feldspar grains (red). Relative orientation of mylonitic S-C fabric shown at upper left. (D) Quartz SGR with grain-shape fabric (GSF), truncated by cataclasite with biotite-rich matrix (yellow) and mylonitic clasts (red). (E) BLG and SGR recrystallization in quartz and SGR in quartz affected by nearby feldspar porphyroclasts (lower part of image). Biotite-rich shear band is present (red). (F) GBM in quartz domains adjacent to recrystallized feldspar. Some quartz grains are pinned at feldspar-quartz grain boundaries (red). (G) SGR in quartz. (H) GSF in quartz exhibiting GBM recrystallization microstructure. (I) BLG (red) and SGR in quartz. White mica forms fish and shear bands (yellow). (J) Quartz exhibiting GBM, deflecting into fine-grained quartz-feldspar-mica shear bands (yellow). Myrmekite (red) grows into K-feldspar porphyroclasts and within matrix. Recrystallized feldspar occurs along plagioclase and K-feldspar porphyroclast edges (white). (K) Orthogonal subgrain boundaries forming chessboard extinction (CB) in quartz.

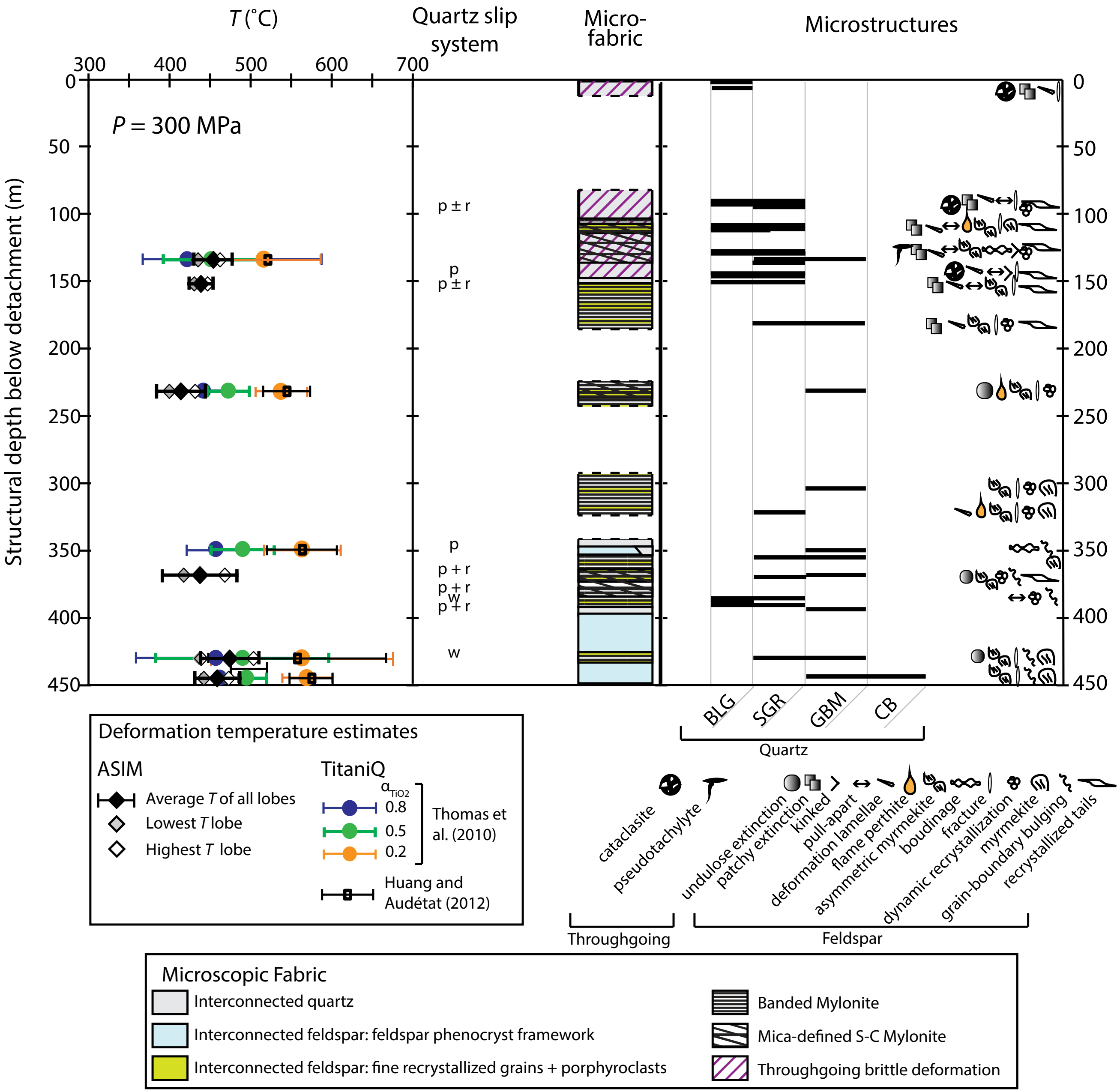

Figure 7. Summary figure of microstructural analysis, geothermometry, and quartz crystallographic preferred orientation results at increasing structural depths below the Cordillera Blanca detachment. Quartz slip systems: p—prism <a>; r—rhomb <a>; w—weak. Deformation temperature (*T*) errors are as reported in Table 2. Error bars for average asymmetric strain-induced myrmekite (ASIM) temperatures do not include the ±50 °C error on the thermometer. *P*—pressure; TitaniQ—Ti-in-quartz thermometer; α_{TiO_2}—Ti activity; BLG—bulging recrystallization; SGR—subgrain rotation recrystallization; GBM—grain-boundary migration recrystallization; CB—chessboard extinction.

S-C mylonites. S-C mylonites are broadly characterized by prominent interconnected quartz domains with S-planes defined primarily by quartz grain-shape fabrics and mica. Type I S-C fabrics as described by Berthé et al. (1979) and Lister and Snoke (1984), where S-surfaces anastomose into and out of C-surfaces and C′-surfaces, are relatively well developed (Figs. 8A, 8B), and type II S-C fabrics, which contain prominent C-surfaces defined by tails of sheared mica fish and S-surfaces defined by quartz grain-shape fabrics (Fig. 8C), are observed in the CBSZ. Quartz in S-C mylonites surrounds isolated feldspar porphyroclasts that contain ASIM or are fractured with quartz infill (Fig. 8C). Biotite or white mica shear bands in some cases have become interconnected, enveloping feldspar porphyroclasts and dynamically recrystallized quartz clasts (Fig. 8D).

Banded mylonites. Banded mylonites comprising interlayered monophase aggregates of quartz or feldspar and polyphase aggregates of feldspar + quartz ± mica up to ~1500 µm thick (Figs. 8E–8I) are observed between 111 and 430 m structural depth (Fig. 7; Table 1). Boundaries between layers tend to align with mesoscopic foliation, which are typically the most prominent foliation surfaces (Fig. 8E). Fine-grained feldspar ± mica bands alternate with monomineralic quartz layers containing microstructures characteristic of SGR and/or GBM recrystallization (Figs. 8F, 5D). Quartz + feldspar domains exhibit relatively equant grain shapes and grain sizes smaller than those of either feldspar or quartz monophase domains, and occur as continuous bands up to ~500 µm thick (Fig. 8G). Domains of finely recrystallized quartz + feldspar + mica appear to originate at plagioclase or K-feldspar porphyroclasts and extend into bands up to ~1.5 mm thick that are continuous at the thin-section to hand-sample scale (Fig. 8H). Fine-grained aggregates contain plagioclase with more albitic composition than porphyroclasts intermixed with K-feldspar, quartz, and biotite (Fig. 8I). K-feldspar occupies dilatant sites and triple junctions within quartz aggregates and between plagioclase grains (Fig. 8I).

Deformation Temperatures

Two-Feldspar Geothermometry

Deformation temperatures derived from ASIM for six samples from structural depths of 134 m to 446 m below the detachment range from 410 ± 30 °C to 470 ± 36 °C (Table 2; Fig. 7). Temperatures do not vary systematically with structural depth and instead overlap within the 50 °C error of the thermometer.

TitaniQ Geothermometry

Deformation temperatures at structural depths from 134 to 446 m are between 451 ± 60 and 489 ± 33 °C, using the Thomas et al. (2010) TitaniQ geothermometer, assuming α_{TiO_2} of 0.5 and 300 MPa pressure. This assumption is made based on the absence in samples of a Ti-bearing phase other than biotite that is in clear equilibrium with quartz. Ti-bearing phases such as rutile and/or ilmenite are present only in three analyzed samples and were either along cleavage planes in biotite or within fractures that cut across recrystallized grain boundaries. The assumed activity of 0.5 is in line with Ti activities determined by geochemical modeling for granitoids of similar composition at similar pressures to the those of the CBSZ (Huang and Audétat, 2012) as well as experimentally grown quartzites where rutile is present but sparse (>200 µm between grains; Nachlas and Hirth, 2015). Ti activities as low as 0.2 have been reported in some plutons as well as volcanic rocks with similar compositions to the Cordillera Blanca batholith (Huang and Audétat, 2012; Kularatne and Audétat, 2014). Temperatures are ~70 °C hotter for α_{TiO_2} of 0.2 and ~30 °C cooler for an activity of 0.8 (Table 2). Temperatures estimated from the Huang and Audétat (2012) TitaniQ calibration range from 520 ± 66 °C to 574 ± 30 °C. These values are within 10 °C of temperatures estimated using the Thomas et al. (2010) calibration for α_{TiO_2} of 0.2 (Fig. 7, Table 2). TitaniQ thermobarometry demonstrates a slight decrease in temperature at decreasing structural depths (Fig. 7). However, this systematic variation is not readily observed with ASIM thermometry (Fig. 7, Table 2). Conservatively, deformation temperatures from TitaniQ thermobarometry are between 451 ± 60 °C and 574 ± 30 °C. TitaniQ temperatures for the CBSZ should be received with caution because, in addition to the uncertainty regarding α_{TiO_2} in the CBSZ, the measured Ti concentrations are at or near the detection limit of ~11 ppm for all samples (see Text S3 [footnote 1] for additional details).

Quartz CPOs

Quartz CPO patterns indicate predominant prism <*a*> and rhomb <*a*> slip (Fig. 9). Most samples from 94 m to 380 m from the detachment show slightly elongated *y*-maxima characteristic of dominant prism <*a*> slip with subsidiary rhomb <*a*> slip. Samples at 384 m and 430 m below the detachment had weak CPOs with M-indices ≤0.07. CPO strength otherwise appears uncorrelated with structural depth or slip system. At 152 m and 369 m, a- and prism-normal-axes do not form the six maxima expected for <*a*> slip and are instead smeared into three dispersed maxima.

Flow Stress

Differential stress, hereafter referred to as “stress”, estimates (Table 3) range from 16.5 ± 13 MPa to 71.5 ± 36 MPa using the Holyoke and Kronenberg (2010) piezometer, measured at 350 m (sample CB13-59) and 149 m (sample CB13-76), respectively (Fig. 10). The structurally highest sample, CB13-77c (94 m), yields a stress of 40.0 ± 22 MPa. The highest stress of 71.5 ± 36 MPa is from the deepest sample that contains throughgoing brittle overprinting of ductile fabrics (sample CB13-76, 149 m). Intermediately positioned sample CB13-78 (152 m) records the next highest stress of 64.3 ± 26 MPa. Sample CB13-59 (350 m)

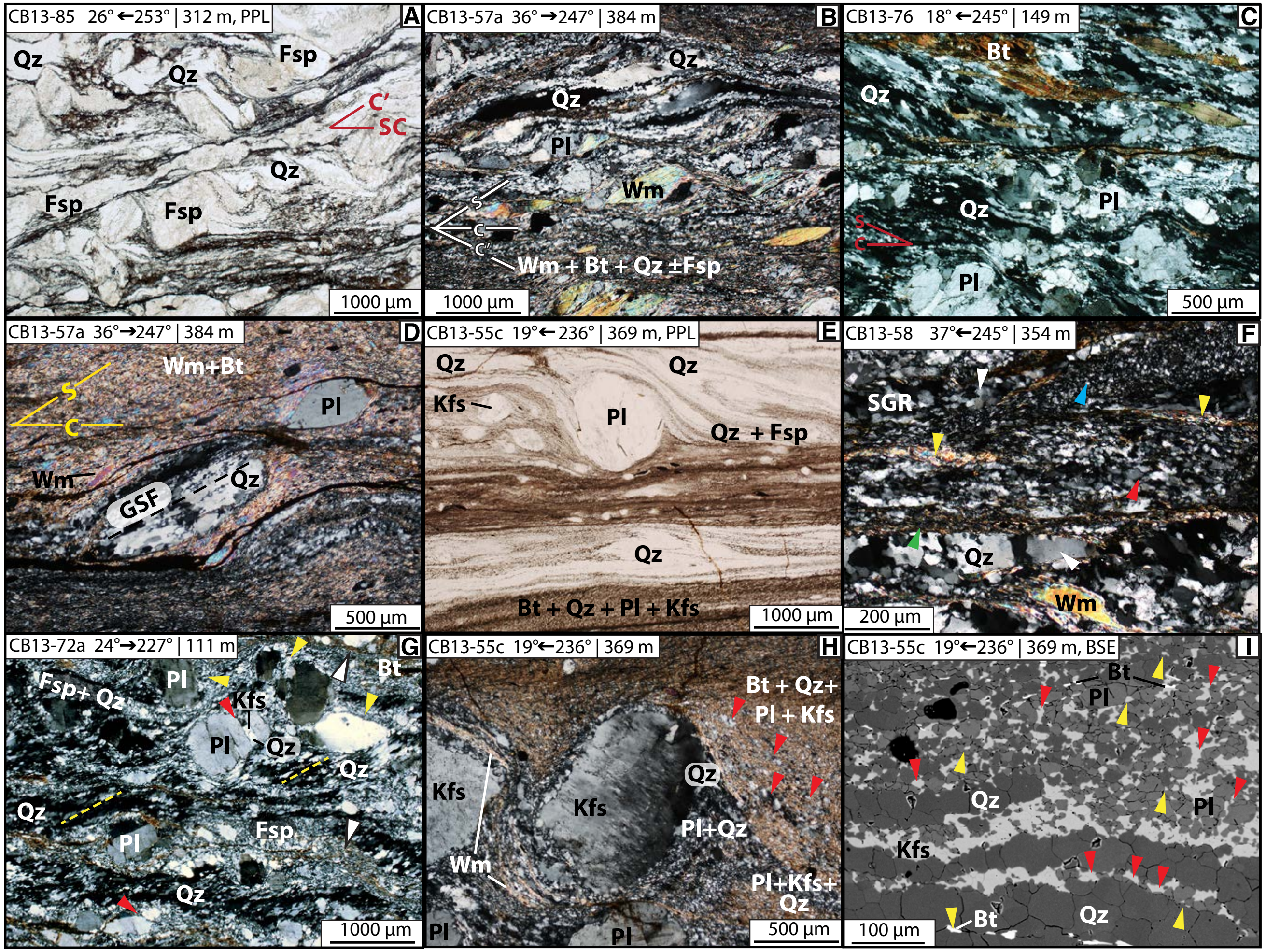

Figure 8. Photomicrographs of microfabrics. Images are cross-polarized light (XPL) unless otherwise noted. Labels denote trend and plunge of lineation, with arrow pointing down-plunge and structural depth below the Cordillera Blanca detachment (in meters); arrowhead indicators are specified below as (color). Bt—biotite; Fsp—feldspar (undifferentiated); Kfs—K-feldspar; Pl—plagioclase; Qz—quartz; Wm—white mica. (A) Plane polarized light (PPL) image of type I S-C mylonite. S-surfaces anastamose in and out of C-surfaces. C′ bands are defined by biotite and finely recrystallized quartz and feldspar. (B) Type I S-C mylonite. S-surfaces defined by mica fish and quartz anastamose into C-surfaces. (C) Type II S-C mylonite. S-surfaces are defined by biotite fish fabric and quartz grain-shape fabric (GSF). Biotite tails define C-surfaces. (D) White mica + biotite shear bands deflecting around recrystallized quartz and plagioclase porphyroclasts. GSF in quartz porphyroclast is aligned with S-plane defined by micas. (E) PPL image of banded mylonite with biotite-rich and biotite-poor, quartz-rich layers. (F) Compositionally banded mylonite with discontinuous mono- and polyphase layers. Monophase layers consist of quartz (white) or white mica (yellow); polyphase layers consist of quartz + plagioclase + K-feldspar (blue), K-feldspar + plagioclase (red), or white mica + quartz + plagioclase + K-feldspar (green). SGR—subgrain rotation. (G) Banded mylonite with continuous quartz layers and feldspar + quartz ± biotite (white) layers deflecting around fractured (red) and partially recrystallized (yellow) plagioclase porphyroclasts. Quartz exhibits oblique GSF (yellow dashed lines). (H) Recrystallization along rim of K-feldspar and plagioclase grains and within tails. Tails disaggregate into fine-grained biotite + quartz + plagioclase + K-feldspar matrix (red). (I) Backscattered electron (BSE) image of intermixed fine-grained polyphase matrix. K-feldspar occupies dilatant sites between plagioclase and quartz grains (red). Biotite and K-feldspar occupy grain boundaries and triple junctions (yellow). Black is result of holes and/or poor polish.

TABLE 2. CALCULATED DEFORMATION TEMPERATURES WITH RESPECT TO STRUCTURAL DEPTH, CORDILLERA BLANCA SHEAR ZONE

				Temperature (°C)							
				TitaniQ*				ASIM			
				Thomas et al. (2010)			Huang and Audétat (2012)				
Sample	Structural depth (m)	Ti (ppm)†	N§	Activity 0.2	Activity 0.5	Activity 0.8		Average#	Highest-T lobe	Lowest-T lobe	N**
CB13-79	134	8 ± 6	34	516 ± 71	451 ± 60	421 ± 55	520 ± 66	450 ± 24	461	434	4
CB13-78	152	–††	–	–	–	–	–	440 ± 15	446	429	3
CB13-84	232	11 ± 4	11	542 ± 32	472 ± 26	441 ± 24	544 ± 29	410 ± 30	429	399	3
CB13-59	350	14 ± 7	59	563 ± 47	489 ± 39	456 ± 36	563 ± 43	–	–	–	–
CB13-55c	369	–	–	–	–	–	–	440 ± 46	467	416	4
CB13-55a	430	13 ± 12	12	556 ± 118	484 ± 99	452 ± 92	557 ± 110	470 ± 36	502	435	14
CB13-54a	446	14 ± 6	53	563 ± 40	489 ± 33	456 ± 30	574 ± 30	460 ± 28	474	441	4

Note: TitaniQ—Ti-in-quartz; ASIM—asymmetric strain-induced myrmekite; *T*—temperature; activity—Ti activity.
*Error shown is Ti concentration uncertainty propagated through the thermometer.
†2σ standard deviation.
§Number of points analyzed.
#Error is 2σ standard deviation of temperatures from all measured lobes.
**Number of myrmekite lobes analyzed. Number of points analyzed per lobe varies between samples (see Table S2 [text footnote 1]).
††–, not determined.

TABLE 3. PALEOPIEZOMETRIC AND STRAIN RATE ESTIMATES, CORDILLERA BLANCA SHEAR ZONE

		Grain size				Differential stress**			Temperature		Strain rate			
Sample	Structural depth (m)	RMS* (µm)	1σ std. dev.† (µm)	Std. err.§ (µm)	N#	HK10†† (MPa)	ST03§§ (MPa)	C17## (MPa)	TitaniQ*** (°C)	ASIM (°C)	TitaniQ††† (s^{-1})	ASIM††† (s^{-1})	TitaniQ§§§ (s^{-1})	ASIM§§§ (s^{-1})
CB13-77c	94	23.5	12.3	0.47	687	40.0 ± 22	54.6 ± 35	61.9 ± 25	–###	–	–	–	–	–
CB13-76****	149	11.3	5.7	0.26	482	71.5 ± 36	97.6 ± 59	98.1 ± 38	451 ± 60	450 ± 24	2.5×10^{-12}	2.6×10^{-12}	3.6×10^{-12}	3.5×10^{-12}
CB13-78	152	12.9	5.4	0.14	1586	64.3 ± 26	87.9 ± 43	90.2 ± 27	–	440 ± 15	–	1.0×10^{-12}	–	1.6×10^{-12}
CB13-59	350	71.7	44.9	3.3	185	16.5 ± 13	22.5 ± 19	30.7 ± 17	489 ± 39	–	2.6×10^{-14}	–	3.5×10^{-14}	–
CB13-55c	369	18.6	9.0	0.3	907	48.2 ± 23	65.8 ± 38	71.7 ± 26	–	440 ± 46	–	3.0×10^{-13}	–	5.1×10^{-13}
CB13-57a	384	15.3	7.2	0.2	1269	56.3 ± 26	76.9 ± 43	81.2 ± 29	–	–	–	–	–	–
CB13-57c	386	14.3	6.7	0.22	977	59.3 ± 27	81.0 ± 45	84.6 ± 30	–	–	–	–	–	–
CB13-55a	430	30.9	14.1	0.72	380	32.1 ± 14	43.9 ± 24	52.0 ± 18	484 ± 99	470 ± 36	3.7×10^{-13}	1.4×10^{-13}	4.3×10^{-13}	2.8×10^{-13}

Note: TitaniQ—Ti-in-quartz; ASIM—asymmetric strain-induced myrmekite.
*Root mean square (RMS) of the grain-size distribution.
†1σ standard deviation of the grain-size distribution.
§Standard error of the grain-size distribution.
#Number of grains within the population used for paleopiezometry.
**Errors are 1σ standard deviation of grain size propagated through the piezometer. Average of stress error above and below RMS (from low and high grain-size errors, respectively) is reported.
††Stress calculated using the Stipp and Tullis (2003) piezometer modified by Holyoke and Kronenberg (2010).
§§Stress calculated using the Stipp and Tullis (2003) piezometer.
##Stress calculated using the Cross et al. (2017b) sliding piezometer calibration.
***TitaniQ temperatures calculated at pressure of 300 MPa, α_{TiO_2} (TiO_2 activity) = 0.5.
†††Calculated using wet quartz flow law of Hirth et al. (2001), $\dot{\varepsilon} = Af^{m}_{H_2O}\sigma^{n}10^{(-Q/RT)}$, where log(*A*) = –11.2 MPa $^{-n}$/s, (*n* is the stress exponent, = 4), *Q* = 135 ± 15 kJ/mol; *m* = 1; *n* = 4; *R* = 8.314 × 10^{-3} kJ/mol·K; f_{H_2O} is water fugacity, assuming water pressure is lithostatic at pressure = 300 MPa, calculated using the fugacity calculator: https://www.esci.umn.edu/people/researchers/withe012/fugacity.htm (Sterner and Pitzer, 1994).
§§§Calculated using wet quartz flow law for prism <a> slip from Tokle et al. (2019), following the same equation as Hirth et al. (2001), but where *A* = 1.75 × 10^{-12} MPa $^{-n}$/s; *Q* = 125 ± 15 kJ/mol; m = 1; n = 4, with *R, T,* and f_{H_2O} as in the Hirth et al. (2001) flow law.
###–, not determined.
****Temperatures derived from nearby sample CB13-79 (134 m).

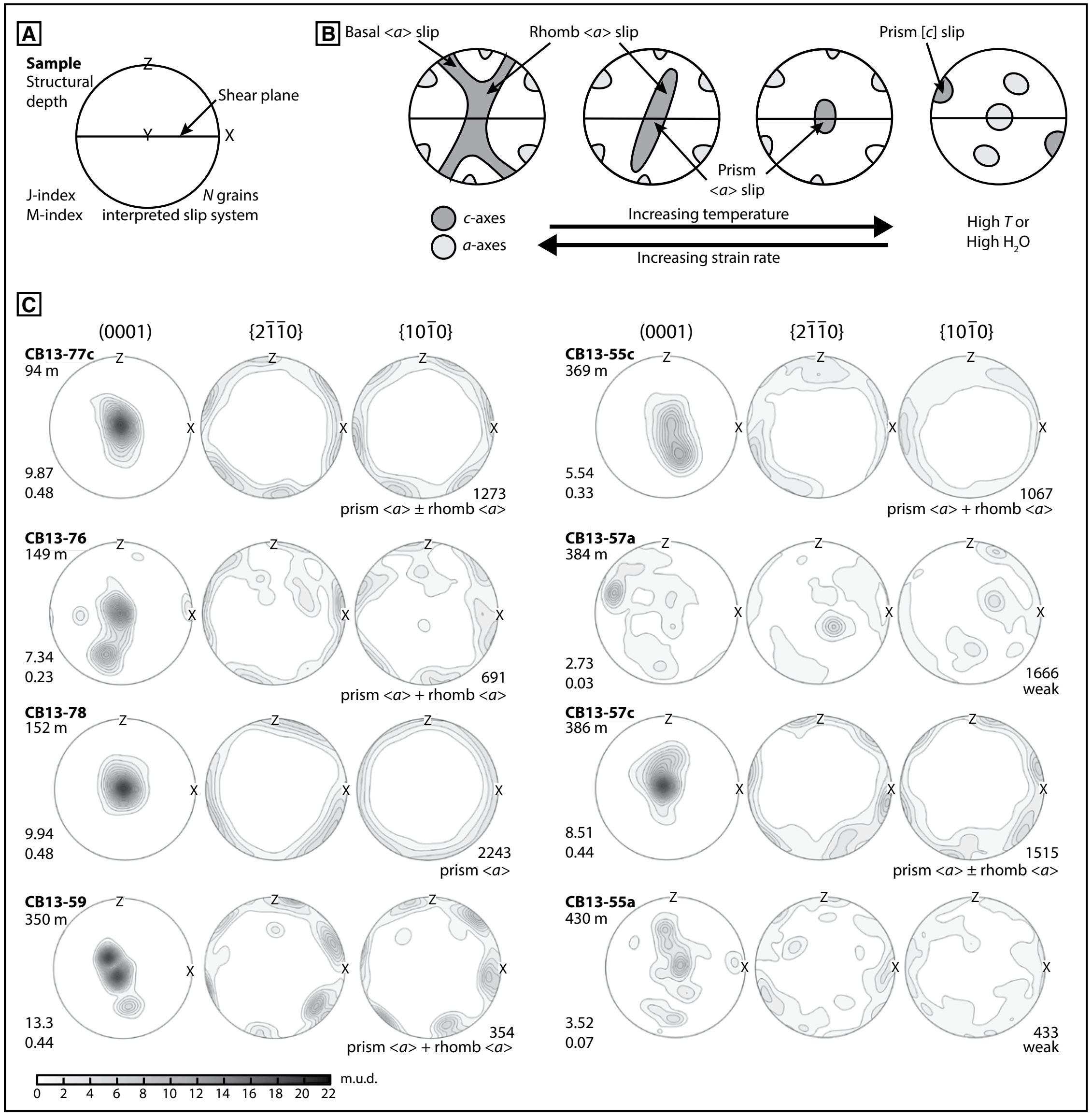

Figure 9. Quartz crystallographic preferred orientations (CPOs). (A) Orientation of quartz CPO pole figures relative to shear plane and *X-Z* thin section, with key to labels for panel C. J-index (Bunge, 1982) and M-index (Skemer et al., 2005) indicate fabric strength. *N*—number of grains. (B) Schematic *c*- and *a*-axis pole figures of quartz CPOs for different quartz slip systems with changing temperature (*T*), strain rate, and H_2O conditions (after Passchier and Trouw, 2005). (C) Equal-area lower-hemisphere pole figures of quartz *c*- (0001), *a*- {2$\bar{1}\bar{1}$0}, and prism-normal- {10$\bar{1}$0} axes. All plots are one point per grain, contoured at 1 m.u.d. (multiple of uniform distribution) intervals, using a 7.5° half-width. Orientation of figures relative to X-Z plane, and labels are as in A.

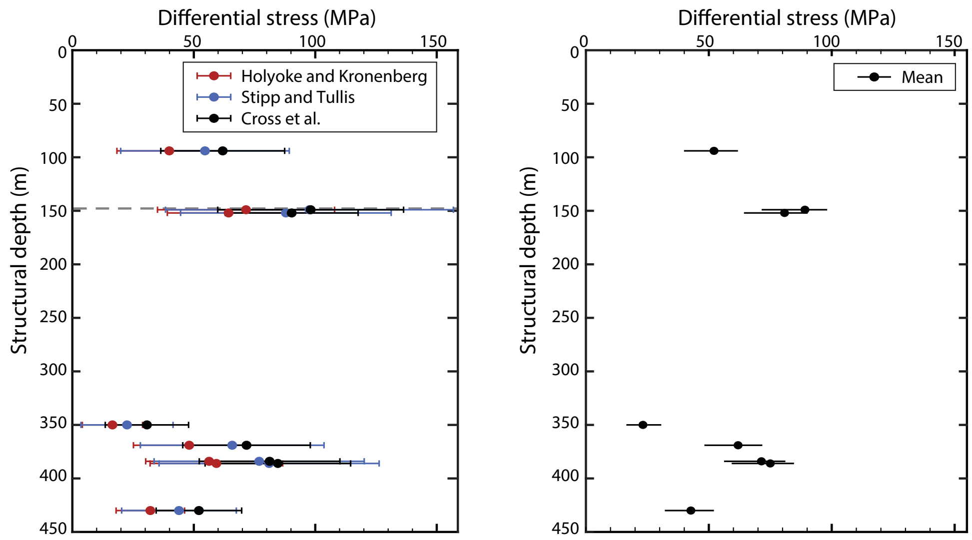

Figure 10. Differential stress estimates with increasing depth below the Cordillera Blanca detachment. (A) Differential stress estimates for Stipp and Tullis (2003), Holyoke and Kronenberg (2010), and Cross et al. (2017b) piezometers, shown relative to structurally deepest observed sample containing throughgoing brittle overprint (gray dashed line). Error bars are standard deviation on root mean square grain size propagated through each piezometer. (B) Mean differential stress of the three piezometers. Error bars are maximum range of stress estimates from the three calibrations.

yields the lowest stress estimate of observed samples, 16.5 ± 13 MPa. Further below the detachment, sample CB13-55c (369 m) yields a stress of 48.2 ± 23 MPa. Stresses calculated at lower structural positions are 56.3 ± 26 MPa and 59.3 ± 27 MPa, from samples CB13-57a (384 m) and CB13-57c (386 m), respectively. The lowest structural position analyzed (sample CB13-55a, 430 m) yields a stress of 32.1 ± 14 MPa. Stress estimates using the Stipp and Tullis (2003) and Cross et al. (2017b) calibrations range from 22.5 ± 19 to 97.6 ± 59 MPa and 30.7 ± 17 to 98.1 ± 38 MPa, respectively and are within error of those calculated using the Holyoke and Kronenberg (2010) calibration (Fig. 10, Table 3). In summary, a consistent gradient in stress as a function of structural depth is not observed; rather, the highest stresses are observed at intermediate structural positions near 150 m where the deepest throughgoing brittle overprinting is observed.

DISCUSSION

Quartz CPOs

It is important to note that CPOs may be inherited from earlier deformation. Strong preexisting growth CPOs in quartz veins have been shown to influence CPOs of quartz veins deformed at lower temperatures, where quartz initially grew in an orientation favorable for easy slip at high temperatures (e.g., prism <*a*> slip at >500 °C) (Pennacchioni et al., 2010). Grains were oriented unfavorably for basal <*a*> slip when temperatures decreased during deformation such that even at relatively low temperatures, strong CPOs indicative of prism <*a*> ± rhomb <*a*> slip were preserved (Toy et al., 2008; Pennacchioni et al., 2010). Previous work also suggests that oriented grain growth during submagmatic flow may influence later CPO development during subsolidus deformation (Zibra et al., 2012). We thus consider the possibility that strong CPOs at positions nearer to the detachment may be inherited from early deformation at relatively high temperatures where prism <*a*> slip was initially favored, or from oriented grain growth during submagmatic flow. The weak fabric in the deepest sample analyzed for EBSD (sample CB13-55a, 430 m) resembles an elongate *y*-axis maximum expected for prism <*a*> ± rhomb <*a*> slip that is seen in stronger CPOs at structurally higher positions (Fig. 9). Although this could suggest some degree of inheritance from a preexisting CPO in the weakly deformed granodiorite, ASIM and TitaniQ estimates suggest that deformation for most of the CBSZ occurred at temperatures above ~400 °C, which is consistent with temperatures where prism <*a*> and rhomb <*a*> slip are expected to occur more readily than basal <*a*> slip (Law et al., 1990; Toy et al., 2008). CPO inheritance is a possibility in the CBSZ but is not required to explain our data.

Deformation Mechanisms

Feldspar

Fracturing. Feldspar exhibits fracturing throughout most of the CBSZ (Fig. 7). At structurally higher positions, fractures occur predominantly in plagioclase porphyroclasts that are surrounded by quartz and/or fine-grained feldspar + quartz ± mica domains. At structurally deep positions, K-feldspar and plagioclase phenocrysts form an interconnected framework that features inter- and intragranular fractures.

Previous studies have documented fracturing at submagmatic to subsolidus conditions in networks of load-bearing interconnected feldspar (Rosenberg, 2001; Zibra et al., 2012; Bessiere et al., 2018). Syn-magmatic fractures in granitoids are characterized by K-feldspar and plagioclase films along grain boundaries at high angles to foliation planes and by fractures filled with at least one phase that would crystallize from a residual melt (Rosenberg, 2001). These characteristics are consistent with those described by Bouchez et al. (1992) for submagmatic fractures at melt fractions between 0.10 and 0.30. Submagmatic fractures are described as those: (1) that transect single grains, (2) that are filled with a phase that is crystallographically and compositionally continuous inside and outside of the fracture, and (3) whose filling phase is expected to crystallize from the residual melt (Bouchez et al., 1992). Within the CBSZ, fractures satisfying these criteria occur at structurally deep positions, where quartz exhibiting the same orientation extends from a wedge-shaped pocket into an adjacent narrow fracture (Fig. 5H, 446 m). The amount of melt required to produce submagmatic fractures has been debated. Melt fractions of 0.3–0.5 had been argued to be required for the formation of throughgoing melt-filled fractures (Arzi, 1978; Paterson et al., 1989), though further investigation into the experimental work from whence these values were derived suggest that melt-filled fractures could be produced at lower melt fractions, potentially as low as 0.07 (Rosenberg and Handy, 2005).

Although quartz crystallization would be consistent with the third criterion above as set forth by Bouchez et al. (1992), other evidence for magmatic deformation or submagmatic deformation, such as imbricated feldspar phenocrysts, is not observed in the CBSZ. The wedge-shaped nature of the quartz exhibiting chessboard extinction is consistent with some degree of rotation of the fractured K-feldspar (Hippertt, 1993), which must have occurred at or above the temperature required for chessboard extinction in quartz (~630 °C; Kruhl, 1996), placing it in the field of high-temperature subsolidus deformation. Alternatively, the quartz exhibiting chessboard extinction may have been late-stage melt filling a pocket between plagioclase and K-feldspar porphyroclasts, with submagmatic fracturing occurring at the melt-porphyroclast interface of the melt pocket at a low melt fraction, still near the boundary between submagmatic and subsolidus conditions (Paterson et al., 1989). In either scenario, evidence for the role of fracturing in feldspar deformation at high temperatures is observed at deepest structural positions within the CBSZ.

Dislocation creep versus cataclastic flow. Deformation experiments on plagioclase single crystals with no initial microstructure other than growth twins suggest that feldspar experiences complex semi-brittle cataclastic flow, where brittle processes (i.e., microfracturing) and plastic processes (i.e., deformation twinning via dislocation climb) are interdependent (McLaren and Pryer, 2001). The coincidence of deformation lamellae with fractured feldspar porphyroclasts and undulose extinction within the upper ~180 m of the CBSZ may suggest the activity of this type of semi-brittle flow. These microstructures are also consistent with those described for cataclastic flow by Tullis and Yund (1987). In their albite aggregate deformation experiments, Tullis and Yund (1987) described characteristic microstructures of cataclastic flow that include undulatory and/or patchy extinction and flattening, grain-scale faults with small offset, and microcracks. The authors noted that patchy undulose extinction, which has also been interpreted to represent dislocation creep (Tullis and Yund, 1977), is typically caused by microcrack arrays and crushed zones visible at the submicron scale.

Evidence for the activity of dislocation creep in feldspar is also observed within the CBSZ. Dynamic recrystallization in feldspar can produce relatively small, rounded, and undeformed feldspar porphyroclasts (Tullis and Yund, 1985). During dislocation creep in feldspar, recrystallization is primarily accommodated by migrating grain boundaries (Tullis and Yund, 1987), producing grain-boundary bulges and small strain-free recrystallized grains (Stünitz et al., 2003) characteristic of BLG recrystalliztion microstructures. Additional related microstructures can include undulatory extinction in relatively equant grains and augen surrounded by a fine-grained matrix at relatively high strains. Undulose extinction due primarily to dislocation creep sweeps continuously across a grain, as opposed to the patchy undulose extinction that can result from dislocation entanglement (Hirth and Tullis, 1992) or cataclastic flow (Tullis and Yund, 1987). Fine, equant, relatively strain-free, recrystallized grains occur along the margins of porphyroclasts, grain boundaries, and fractures, commonly extending out into tails under high strains (Tullis and Yund, 1985).

Within the CBSZ, fine recrystallized feldspar occurs at a wide range of structural depths (92–446 m; Table 1; Fig. 7). As these microstructures may be formed by either cataclastic flow or dislocation creep, interpreting deformation mechanisms by singular microstructures alone is difficult. Here, interpretation of the activity of dislocation creep in feldspar is limited to samples where grain-boundary bulges can be observed (i.e., Fig. 5E) and where undulatory extinction, if present, is continuous across grains rather than patchy. If patchy undulose extinction occurs, especially if coinciding with kinked or bent twins or cleavage planes, or pull-apart–type fractures, the prominent deformation mechanism is interpreted to be cataclastic flow. Under these considerations, dislocation creep in feldspar likely occurred at relatively deep structural positions (350 m to 446 m), suggesting deformation temperatures above ~450 °C (Yund and Tullis, 1980), consistent with ASIM-derived temperatures of 440 ± 46 to 470 ± 36 °C and TitaniQ temperatures of 484 ± 99 to 489 ± 39 °C (Thomas et al. [2010] calibration; α_{TiO_2} = 0.5) for the same structural positions (Fig. 10). Alternatively, cataclastic flow likely occurred at structural positions above ~350 m. This relationship may be oversimplified, as a cataclastic overprint (in feldspar) could reduce evidence for dislocation creep, but also more simply because of the similarity of microstructures between cataclastic flow and dislocation creep (i.e., Tullis and Yund, 1987).

Quartz

Dislocation creep. Recrystallization microstructures and CPOs can be used to distinguish between prominent deformation mechanisms (Hirth and Tullis, 1992; Stipp et al., 2002b). Recrystallized quartz CPOs mainly show patterns indicative of dominant prism <*a*> slip with variable lesser contributions of rhomb <*a*> slip, which is consistent with quartz dislocation creep at 94–386 m below the detachment surface (Fig. 9). Previous studies suggest that temperature is the primary contributing factor to activating different slip systems in quartz aggregates, with the transition from basal slip to prism slip occurring at high temperatures (Tullis et al., 1973; Mainprice et al., 1986; Morales et al., 2011). Above ~500 °C, prism <*a*> occurs as the dominant slip system, and at increasingly high temperatures of ~600 °C, slip in the <*a*> direction gives way to dominant prism [*c*] slip (Mainprice et al., 1986; Schmid and Casey, 1986; Kruhl, 1996; Passchier and Trouw, 2005). However, transitions between dominant slip mechanisms inferred from quartz CPOs may also be affected by changes of strain rate and/or the activity of water within the shear zone (Fig. 9; Mainprice and Paterson, 1984; Stipp et al., 2002b; Mancktelow and Pennacchioni, 2004; Law, 2014; Morales et al., 2014). Excluding the weak fabrics of samples CB13-57a and CB13-55a (384 and 430 m, respectively), quartz CPOs indicate predominant activity of prism <*a*> slip and rhomb <*a*> slip, which are consistent with dislocation creep in quartz at >400 °C (Schmid and Casey, 1986; Stipp et al., 2002a, 2002b; Stünitz et al., 2003).

Grain-boundary sliding. Weak CPOs at 384 and 430 m depth, as well as dispersed *a*-axis maxima at 152 m and 369 m depth, may suggest the activity of other deformation mechanisms, such as diffusion creep and/or grain-boundary sliding (GBS) (Bestmann and Prior, 2003; Wightman et al., 2006; Cross et al., 2017a) or relatively low amounts of accumulated strain (Lister and Hobbs, 1980; Toy et al., 2008). Diffusion creep is unlikely in coarse-grained quartz aggregates (Rutter and Brodie, 2004), such as those in sample CB13-55a (430 m). The weak CPO in sample CB13-55a more plausibly reflects relatively low strain, which is within reason for its deep structural position (430 m) relative to the detachment fault. This relationship is consistent with weak CPOs at positions structurally removed from the main detachment and/or shear zone in other natural settings (Haertel et al., 2013; Haertel and Herwegh, 2014) or in low finite strains in numerical models (Keller and Stipp, 2011; Lister and Hobbs, 1980).

The weak CPO at 384 m (sample CB13-57a) and the dispersed *a*-axis patterns at 152 and 369 m depth (samples CB13-78 and CB13-55c, respectively) may reflect GBS. Dispersed CPO patterns are often attributed to GBS (Jiang et al., 2000; Bestmann and Prior, 2003; Storey and Prior, 2005; Warren and Hirth, 2006; Cross et al., 2017a). Microstructures such as four-grain junctions, square or rectangular grain shapes, alignment of multiple grain boundaries parallel to foliation, and recrystallized grains smaller than subgrains are thought to be indicative of GBS (Halfpenny et al., 2012; Miranda et al., 2016; Rahl and Skemer, 2016). CPOs of sub-populations at 384 m (sample CB13-57a) show that the weak *c*-axis maxima derive mainly from relict grains and that recrystallized grains have dispersed orientations (Fig. S2 [footnote 1]). In this sample, four-grain junctions associated with square grain shapes and alignment of edges across multiple grains also occur within the finer recrystallized population (Fig. S2). These observations, in addition to the dispersion of the CPOs in the fine-grained recrystallized quartz population, are consistent with the activity of GBS in quartz (Bestmann and Prior, 2003; Halfpenny et al., 2006; Wightman et al., 2006; Gan et al., 2007; Kilian et al., 2011; Cross et al., 2017a).

Polyphase Domains

Microstructural observations suggest that polyphase quartz + feldspar ± mica domains may be promoted by phase mixing via GBS, dynamic recrystallization, and pressure-solution creep. Precipitation of soluble phases such as K-feldspar or quartz in dilatant openings, such as in recrystallized porphyroclast tails or pull-apart zones in fine-grained aggregates, has previously been interpreted to represent GBS (Behrmann and Mainprice, 1987; Kilian et al., 2011; Platt, 2015). At least local GBS is supported by K-feldspar in dilatant sites and at triple junctions within quartz aggregates and between plagioclase grains (Fig. 8I; e.g., Stünitz and Tullis, 2001; Fusseis et al., 2009; Oliot et al., 2014; Menegon et al., 2015; Spruzeniece and Piazolo, 2015; Czaplińska et al., 2015; Viegas et al., 2016). Disaggregation of dynamically recrystallized feldspar porphyroclast tails into polyphase quartz + plagioclase + K-feldspar ± biotite domains (Fig. 8H) is consistent with microstructures inferred to form from precipitation in dilatant openings following dynamic recrystallization in porphyroclast tails, where rotation of grains opens up pore space that is subsequently filled by K-feldspar (Kilian et al., 2011; Platt, 2015).

Strain Rates

Strain rates derived from the wet quartz flow law of Hirth et al. (2001) are 2.6×10^{-14} to 2.6×10^{-12} s^{-1} using stresses derived from the Holyoke and Kronenberg (2010) piezometer and temperatures from TitaniQ ($\alpha_{TiO_2} = 0.5$) and ASIM thermometry. Similar strain rates of 3.5×10^{-14} to 3.6×10^{-12} s^{-1} are obtained using the new quartz flow law for prism <a> slip (Tokle et al., 2019) (Table 3). Strain rates increase to 3.1×10^{-13} to 9.4×10^{-12} using the Cross et al. (2017b) piezometer. Highest calculated strain rates (2–9 × 10^{-12} s^{-1}) are from ~150 m below the detachment, near the position of the deepest throughgoing brittle overprint. Displacement of 12–15 km along the detachment since ca. 5 Ma (Bonnot, 1984; Giovanni, 2007; Giovanni et al., 2010) yields a time-averaged slip rate of 2.4–3 mm/yr. If it is assumed that the width of the shear zone between a given sample and the detachment was active during shear zone evolution, shear zone widths prior to onset of brittle deformation were between ~450 m and ~150 m. These widths correspond to time-averaged strain rates from 1.7 to 6.3×10^{-13} s^{-1} for 450 and 150 m widths, respectively, under the assumption that strain rate = velocity / width (Platt and Behr, 2011b). Despite uncertainties in temperature and stress values, strain rates estimated from individual samples generally agree with the time-averaged strain rate for the CBSZ.

Use of ASIM temperatures in the quartz flow law requires a simplified assumption that myrmekite formation and quartz deformation are coeval. TitaniQ temperatures at $\alpha_{TiO_2} = 0.5$ overlap with ASIM temperatures within error (Fig. 7;

Table 2), supporting the use of ASIM temperatures as an approximation of deformation temperatures in quartz for strain rate calculations when quartz-based temperature data are unavailable. ASIM temperatures are broadly consistent with temperatures >400 °C inferred from quartz CPOs as well as temperatures expected for SGR recrystallization (400–500 °C; Stipp et al., 2002a), and are within error of the transition to GBM recrystallization at strain rates of ~10^{-12} s^{-1} (480–530 °C; Stipp et al., 2002a). TitaniQ analyses were selectively conducted on samples with GBM recrystallization microstructures, which at strain rates of ~10^{-12} s^{-1} occur at temperatures >500 °C (Stipp et al., 2002a). ASIM temperatures and TitaniQ temperatures for these samples, while in agreement with each other at α_{TiO_2} = 0.5, are below the expected range from Stipp et al. (2002a). Deformation experiments suggest that one-order-of-magnitude variation in strain rate has a similar effect on recrystallization microstructure to a 200 °C shift in temperature, and that an increase in water content changes recrystallization microstructures in a similar matter to an increase in temperature (Stipp et al., 2006).

Shear Zone Evolution

Based on overprinting relationships and structural position relative to the detachment fault, we propose a conceptual model for the evolution of the CBSZ during post-magmatic cooling. In this model, initial deformation in the CBSZ was accommodated by high-temperature feldspar fracturing. Continuing subsolidus deformation occurred at temperatures above ~400 °C through varying contributions of dislocation creep in feldspar, dislocation creep in quartz, cataclasis in feldspar, and at least locally by GBS in polyphase aggregates composed of quartz + feldspar ± mica. The evolution of these mechanisms in the CBSZ does not follow a single progression. Rather, our data support a conceptual model where banded mylonites and/or interconnected quartz domains formed as a result of multiple deformation mechanisms that likely reflect changes in temperature, strain rate, and presence of fluids prior to the onset of throughgoing brittle deformation (Fig. 11).

Initial Deformation

Earliest deformation occurred via fracturing and neocrystallization of K-feldspar and plagioclase and dislocation creep in quartz (Fig. 11A). Chessboard extinction in quartz within submagmatic, intragranular K-feldspar fractures (Figs. 5H, 11A) represents the onset of subsolidus deformation at >630 °C (Kruhl, 1996). Quartz with chessboard extinction and large grains with amoeboid grain boundaries and undulose extinction indicative of GBM recrystallization are common within isolated pockets at the interstices between feldspar phenocrysts. As such, these quartz domains are interpreted to be passive markers of deformation conditions, and rheology is inferred to be controlled by the interconnected network of feldspar phenocrysts.

Grain-Size Reduction

Grain-size reduction of the feldspar network occurred by dislocation creep in plagioclase, recrystallization to fine-grained feldspar or feldspar + quartz along intragranular fractures in K-feldspar phenocrysts, and myrmekite growth (Figs. 5I, 5J, 11A). BLG recrystallization occurs along fractures and the rims of magmatic plagioclase and K-feldspar grains (Fig. 5E, 5I), suggesting that deformation was partially accommodated by dislocation creep in feldspar during early stages of shear zone evolution. Dissolution along plagioclase and K-feldspar fractures facilitated by aqueous fluids is inferred from the crystallization of finer-grained, more sodic feldspar grains along these sites (Fitz Gerald and Stünitz, 1993; Fusseis and Handy, 2008; Viegas et al., 2016). At structurally deep positions within the CBSZ, prominent myrmekite growth along K-feldspar boundaries that is associated with white mica and quartz (Figs. 5J, 11A) also supports the role of fluids in early grain-size reduction of the load-bearing feldspar network (Menegon et al., 2006; Ree et al., 2005; Tsurumi et al., 2002). The presence of white mica and quartz along the inferred original K-feldspar edge supports myrmekite growth facilitated by a local addition of water, where excess K^+ is released and myrmekite and muscovite are formed at the expense of K-feldspar following the reaction (Phillips et al., 1972):

$$\underbrace{\left\{\begin{array}{c}3KAlSi_3O_8\\ NaAlSi_3O_8\end{array}\right\}}_{\text{alkali feldspar}} + \underbrace{\left\{\begin{array}{c}CaAl_2Si_2O_8\\ NaAlSi_3O_8\end{array}\right\}}_{\text{calcic plagioclase}} + \underbrace{H_2O}_{\text{water}} \rightarrow$$

$$\underbrace{\left\{\begin{array}{c}CaAl_2Si_2O_8\\ 2NaAlSi_3O_8\end{array}\right\}}_{\text{more sodic plagioclase}} + \underbrace{6SiO_2}_{\text{quartz}} + \underbrace{KAl_2(Al,Si_3)O_{10}(OH)_2}_{\text{muscovite}} + K_2O\,. \quad (6)$$

Collectively, these observations suggest a role of fluids in promoting grain-size reduction via fracturing, recrystallization, and myrmekite formation within an initially interconnected network of feldspar phenocrysts at >400 °C within the CBSZ.

Interconnection of Quartz Domains

Quartz deformed by dislocation creep in interconnected networks around other isolated phases at a wide range of structural depths in the CBSZ (Fig. 7). The transition from a coarse-grained feldspar network to interconnected quartz network (Fig. 11B) is preserved at 350 m structural depth (i.e., sample CB13-59, Figs. 5E–5G, 6H), where quartz exhibits GBM recrystallization microstructures and plagioclase is boudinaged. The tapered, relatively symmetric nature of plagioclase boudins suggests that quartz was less competent than feldspar,

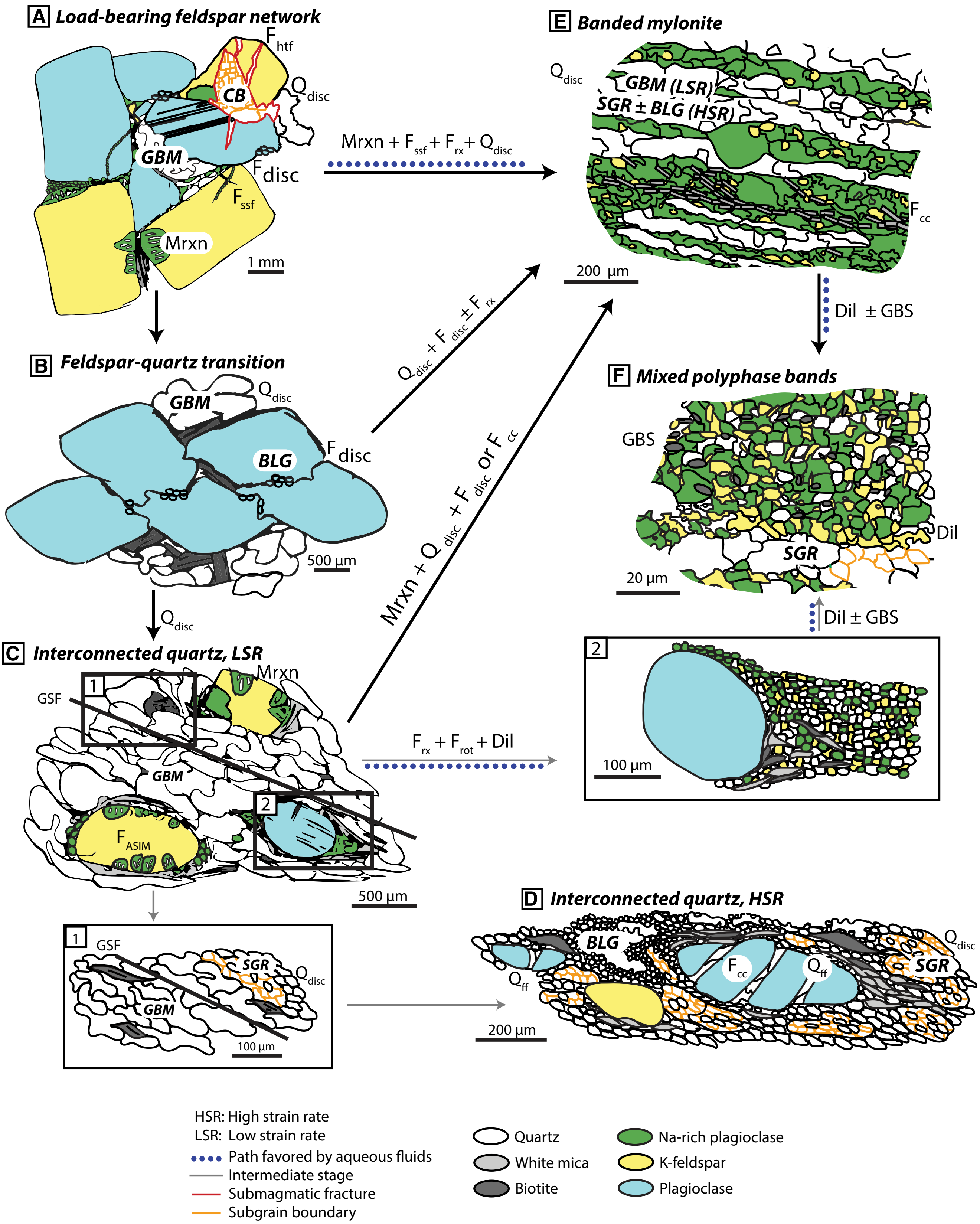

Figure 11. Schematic line drawings summarizing evolution of deformation mechanisms and related microstructures in the Cordillera Blanca shear zone. Arrows denote possible microstructural progressions, labeled with processes facilitating change in microstructure. Gray arrows denote transitional microstructures and processes. Abbreviations: F—feldspar, Q—quartz; htf—high-temperature fracturing; ssf—subsolidus fracturing; disc—dislocation creep; rot—rotation; rx—reaction to Na-rich plagioclase; ff—fracture fill; cc—cataclasis; Mrxn—myrmekite-forming reaction; CB—chessboard extinction; GBM—grain-boundary migration recrystallization; BLG—bulging recrystallization; SGR—subgrain rotation recrystallization; ASIM—asymmetric strain-induced myrmekite; GSF—grain-shape fabric; GBS—grain-boundary sliding; Dil—dilation. Scale bars are approximate. For clarity, grain sizes of quartz in D are depicted as slightly larger than actual. See text for details.

and flowed into boudin necks (Goscombe et al., 2004). As plagioclase within this sample also exhibits BLG recrystallization (Fig. 5E), deformation at the transition from a coarse-feldspar network to a quartz network is consistent with the model for a two-phase system in which both rheological phases deform viscously (i.e., Handy et al., 1999, their figure 1b). In the CBSZ, this transition occurred under relatively low stress (16.5 ± 13 MPa in quartz) near ~500 °C, at the lowest strain rate estimated for individual samples, ~3 × 10^{-14} s^{-1}. Similar differential stresses are reported for extensional mylonitic granitoids exhibiting microstructures indicative of GBM recrystallization in quartz and plastic deformation in feldspar in the core (10–16 MPa) and mylonitic front (~16 MPa) of the Whipple Mountains metamorphic core complex (California, USA) in the North American Cordillera (Behr and Platt, 2011; Cooper et al., 2017).

Deformation within interconnected quartz domains proceeded predominantly by dislocation creep. GBM, SGR, or SGR + GBM recrystallization microstructures in quartz occur at structural positions deeper than ~150 m below the detachment (Fig. 11C), whereas SGR ± BLG recrystallization microstructures primarily occur at structural positions shallower than ~150 m (Fig. 11D), with the exception of a relatively narrow zone at ~385 m depth (Fig. 7). These microstructures are accompanied by quartz CPOs that mainly show strong fabrics indicative of prism <*a*> slip and subsidiary rhomb <*a*> slip, consistent with quartz dislocation creep at >400 °C. The shift in GBM to BLG recrystallization microstructures in addition to SGR microstructures at ~150 is likely due to increasing strain rate. This microstructural transition is often attributed to decreasing temperature, where GBM recrystallization occurs above ~500 °C, and BLG recrystallization occurs below ~400 °C (Stipp et al., 2002b). However, estimated deformation temperatures in the CBSZ are consistently >400 °C and within ~70 °C of each other, suggesting that temperature is likely not the main contributing factor in microstructural evolution. Furthermore, a change in temperature alone would not explain the narrow zone of BLG recrystallization microstructures near ~385 m depth, as temperature changes would be expected to be of relatively large scale due to pluton cooling and/or exhumation of the shear zone along the detachment. Although strain rate could only be derived for a limited number of samples, strain rates estimated for samples near the ~150 m microstructural transition with differential stresses of ~70 MPa (3 × 10^{-12} s^{-1}; samples CB13-76, CB13-78) are an order of magnitude higher than those estimated in deeper positions, supporting the role of strain rate in shear zone evolution. Strain rate estimates near ~150 m in the CBSZ are similar to the upper range of those calculated for the Ruby Mountains core complex (Nevada, USA; 10^{-11} to 10^{-13} s^{-1}) at similar differential stresses (~64 MPa) (Hacker et al., 1990).

Layering of Banded Mylonites

Layering of banded mylonites (Fig. 11E) occurs at depths ranging from 430 m to 111 m (Fig. 7). Formation of layered mylonites in granitoids has previously been attributed to reaction weakening associated with myrmekite formation and recrystallization of myrmekite (Ishii et al., 2007; Menegon et al., 2008) or to cataclastic deformation in feldspar (Pryer, 1993; Hippertt, 1998; Viegas et al., 2016). Unlike with myrmekite formation, development of banded mylonites by cataclastic deformation can occur solely through brittle breakdown of feldspar with no reaction products (Viegas et al., 2016). The deepest banded mylonite (sample CB13-55a, 430 m) records a transition from a coarse-grained feldspar network (Figs. 11A, 11B) to banded mylonite (Fig. 11E) at ~470 °C and moderately low stress (32.1 ± 14 MPa), corresponding to a strain rate of ~1 × 10^{-13} s^{-1}. In this sample, K-feldspar porphyroclasts with asymmetric strain-induced myrmekite have recrystallized tails that deflect into feldspar-rich layers. This transition, in addition to the abundance of myrmekite within the CBSZ along K-feldspar porphyroclasts and also within feldspar C-bands (Figs. 7, 8D), suggests that myrmekite reaction, rather than cataclastic deformation, was the main process that contributed to layering of banded mylonites within the CBSZ.

Development of polyphase domains within banded mylonites (Fig. 11F; i.e., sample CB13-55c, 369 m) may be promoted by dilation and precipitation accompanied by GBS. Dissolution and precipitation in polyphase domains within this sample are inferred from K-feldspar filling dilatant sites between fine recrystallized quartz as well as from biotite and K-feldspar at quartz and plagioclase triple junctions. K-feldspar dissolution is reasonable in this scenario considering the abundance of myrmekite within the CBSZ (Fig. 7) and the excess K_2O produced in the myrmekite-forming reaction (Equation 6; Ishii et al., 2007). This type of behavior and microstructure is consistent with disaggregation of monophase domains by dynamic recrystallization, dissolution and precipitation in dilatant sites opened by rotation, and GBS (Kilian et al., 2011; Platt, 2015). Quartz domains also support a possible role of GBS, as the CPOs show smeared *a*-axes with three dispersed maxima, consistent with the activity of GBS (Cross et al., 2017a). Polygonal subgrains consistent with SGR recrystallization in quartz with a strong *y*-maximum *c*-axis orientation indicate that dislocation creep with preferential prism <*a*> slip was also active, perhaps suggesting that quartz deformation at least locally was accommodated by a combination of GBS and dislocation creep, or DisGBS (i.e., Miranda et al., 2016).

CONCLUSIONS

1. The Cordillera Blanca shear zone (CBSZ) preserves an ~450-m-thick extensional shear zone characterized by undeformed granite in the core of the Cordillera Blanca batholith and increasingly mylonitized fabrics toward the western margin of the batholith. Brittle deformation occurs in the uppermost ~150 m, as evidenced by pseudotachylyte, fault breccia, and cataclasite, and culminates in a moderate- to low-angle normal detachment fault.
2. Deformation along the CBSZ was initiated at near-solidus conditions above ~630 °C in weakly deformed granodiorite at the structurally lowest position relative to the discrete detachment fault, and continued to subsolidus conditions by fracturing of feldspar phenocrysts, dislocation creep, and neocrystallization of fine-grained feldspar along with growth

of myrmekite. Initial interconnection of quartz domains occurred at temperatures near 500 °C under low stress (16.5 ± 13 MPa). Layering of mylonites at structurally deep positions occurred at 470 ± 50 °C where quartz recrystallized via grain-boundary migration and subgrain rotation processes during deformation by dislocation creep. Myrmekite growth contributed to the formation of banded mylonites with quartz monophase and quartz + feldspar ± mica polyphase domains. Dissolution and precipitation in dilatant sites may also have played a role in formation of layered mylonites and at least locally contributed, along with grain-boundary sliding, to formation of fine-grained, mixed quartz + K-feldspar + Na-feldspar + biotite domains.

3. Quartz deformed predominantly by dislocation creep between 400 and 500 °C, producing strong crystallographic preferred orientations indicative of prism <*a*> slip and rhomb <*a*> slip. Variations in differential stress estimates despite similar deformation temperatures across the shear zone suggest that strain rate, rather than temperature, may have been more important in shear zone evolution for the CBSZ.
4. Throughgoing brittle fabrics overprint ductile quartz-rich fabrics within the upper ~150 m. Differential stresses from the CBSZ are consistent with estimates from granitoids in other extensional settings such as the Ruby Mountains and Whipple Mountains core complexes in the North American Cordillera. The highest differential stress in the CBSZ was recorded by the deepest sample within the shear zone to preserve a throughgoing brittle overprint of ductile fabrics, indicating that within the CBSZ, rocks have a strength of at least 71.5 ± 36 MPa at the ductile to brittle transition.

ACKNOWLEDGMENTS

We thank Andrew Cross and John Platt for thorough and constructive reviews. Quartz reference materials were graciously provided by W. Nachlas. We thank J. Mauch for sampling support in the field, along with L. Kellerman at the Montana State University Imaging and Chemical Analysis Laboratory for technical assistance in acquiring EBSD data, and A. Patchen at the University of Tennessee for assistance in acquiring EPMA data. J. Langille assisted with drafting of the modified Giovanni et al. (2010) map. A. Cafferata of Caraz, Peru, and J. Olaza of Huaraz, Peru, aided in field expeditions. This work would not have been possible without funding support from the U.S. National Science Foundation through grant EAR-1220237 to M. Jessup and grant EAR-1220216 to C. Shaw. TitaniQ geothermometry was funded by the Sigma Xi Grant-in-Aid of Research program, awarded to C. Hughes.

REFERENCES CITED

Arzi, A.A., 1978, Critical phenomena in the rheology of partially melted rocks: Tectonophysics, v. 44, p. 173–184, https://doi.org/10.1016/0040-1951(78)90069-0.

Atherton, M.P., and Sanderson, L.M., 1987, The Cordillera Blanca Batholith: A study of granite intrusion and the relation of crustal thickening to peraluminosity: Geologische Rundschau, v. 76, p. 213–232, https://doi.org/10.1007/BF01820584.

Bachmann, F., Hielscher, R., and Schaeben, H., 2010, Texture analysis with MTEX—Free and open source software toolbox: Solid State Phenomena, v. 160, p. 63–68, https://doi.org/10.4028/www.scientific.net/SSP.160.63.

Behr, W.M., and Platt, J.P., 2011, A naturally constrained stress profile through the middle crust in an extensional terrane: Earth and Planetary Science Letters, v. 303, p. 181–192, https://doi.org/10.1016/j.epsl.2010.11.044.

Behr, W.M., and Platt, J.P., 2014, Brittle faults are weak, yet the ductile middle crust is strong: Implications for lithospheric mechanics: Geophysical Research Letters, v. 41, p. 8067–8075, https://doi.org/10.1002/2014GL061349.

Behr, W.M., Thomas, J.B., and Hervig, R.L., 2011, Calibrating Ti concentrations in quartz for SIMS determinations using NIST silicate glasses and application to the TitaniQ geothermobarometer: The American Mineralogist, v. 96, p. 1100–1106, https://doi.org/10.2138/am.2011.3702.

Behrmann, J.H., and Mainprice, D.H., 1987, Deformation mechanisms in a high-temperature quartz-feldspar mylonite: Evidence for superplastic flow in the lower continental crust: Tectonophysics, v. 140, p. 297–305, https://doi.org/10.1016/0040-1951(87)90236-8.

Berthé, D., Choukroune, P., and Jegouzo, P., 1979, Orthogneiss, mylonite and non coaxial deformation of granites: The example of the South Armorican Shear Zone: Journal of Structural Geology, v. 1, p. 31–42, https://doi.org/10.1016/0191-8141(79)90019-1.

Bessiere, E., Rabillard, A., Précigout, J., Arbaret, L., Jolivet, L., Augier, R., Menant, A., and Mansard, N., 2018, Strain localization within a syntectonic intrusion in a back-arc extensional context: The Naxos monzogranite (Greece): Tectonics, v. 37, p. 558–587, https://doi.org/10.1002/2017TC004801.

Bestmann, M., and Prior, D.J., 2003, Intragranular dynamic recrystallization in naturally deformed calcite marble: Diffusion accommodated grain boundary sliding as a result of subgrain rotation recrystallization: Journal of Structural Geology, v. 25, p. 1597–1613, https://doi.org/10.1016/S0191-8141(03)00006-3.

Bonnot, D., 1984, Neotectonique et tectonique active de la Cordillere Blanche et du Callejon de Huaylans (Andes nord-péruviennes) [Ph.D. thesis]: Paris, University de Paris-Sud, 123 p.

Bonnot, D., Sébrier, M., and Mercier, J., 1988, Évolution géodynamique plio-quaternaire du bassin intra-cordillérain du Callejon de Huaylas et de la Cordillère Blanche, Pérou: Géodynamique, v. 3, p. 57–83.

Bouchez, J.L., Delas, C., Gleizes, G., Nédélec, A., and Cuney, M., 1992, Submagmatic microfractures in granites: Geology, v. 20, p. 35–38, https://doi.org/10.1130/0091-7613(1992)020<0035:SMIG>2.3.CO;2.

Brace, W.F., and Kohlstedt, D.L., 1980, Limits on lithospheric stress imposed by laboratory experiments: Journal of Geophysical Research, v. 85, p. 6248–6252, https://doi.org/10.1029/JB085iB11p06248.

Bunge, H.-J., 1982, Texture Analysis in Materials Science: Mathematical Methods (English [second] edition): London, Butterworths, 593 p.

Byerlee, J., 1978, Friction of rocks: Pure and Applied Geophysics, v. 116, p. 615–626, https://doi.org/10.1007/BF00876528.

Carter, N.L., and Tsenn, M.C., 1987, Flow properties of continental lithosphere: Tectonophysics, v. 136, p. 27–63, https://doi.org/10.1016/0040-1951(87)90333-7.

Cobbing, E.J., Pitcher, W.S., Wilson, J.J., Baldock, J.W., Taylor, W.P., McCourt, W., and Snelling, N.J., 1981, The Geology of the Western Cordillera of Northern Peru: London, UK, Institute of Geological Services, 144 p.

Columbu, S., Cruciani, G., Fancello, D., Franceschelli, M., and Musumeci, G., 2015, Petrophysical properties of a granite-protomylonite-ultramylonite sequence: Insight from the Monte Grighini shear zone, central Sardinia, Italy: European Journal of Mineralogy, v. 27, p. 471–486, https://doi.org/10.1127/ejm/2015/0027-2447.

Cooper, F.J., Platt, J.P., and Behr, W.M., 2017, Rheological transitions in the middle crust: Insights from Cordilleran metamorphic core complexes: Solid Earth, v. 8, p. 199–215, https://doi.org/10.5194/se-8-199-2017.

Cross, A.J., Kidder, S., and Prior, D.J., 2015, Using microstructures and TitaniQ thermobarometry of quartz sheared around garnet porphyroclasts to evaluate microstructural evolution and constrain an Alpine Fault Zone geotherm: Journal of Structural Geology, v. 75, p. 17–31, https://doi.org/10.1016/j.jsg.2015.02.012.

Cross, A.J., Hirth, G., and Prior, D.J., 2017a, Effects of secondary phases on crystallographic preferred orientations in mylonites: Geology, v. 45, p. 955–958, https://doi.org/10.1130/G38936.1.

Cross, A.J., Prior, D.J., Stipp, M., and Kidder, S., 2017b, The recrystallized grain size piezometer for quartz: An EBSD-based calibration: Geophysical Research Letters, v. 44, p. 6667–6674, https://doi.org/10.1002/2017GL073836.

Czaplińska, D., Piazolo, S., and Zibra, I., 2015, The influence of phase and grain size distribution on the dynamics of strain localization in polymineralic rocks: Journal of Structural Geology, v. 72, p. 15–32, https://doi.org/10.1016/j.jsg.2015.01.001.

Fitz Gerald, J.D., and Stünitz, H., 1993, Deformation of granitoids at low metamorphic grade. I: Reactions and grain size reduction: Tectonophysics, v. 221, p. 269–297, https://doi.org/10.1016/0040-1951(93)90163-E.

Fukuda, J.I., Okudaira, T., Satsukawa, T., and Michibayashi, K., 2012, Solution-precipitation of K-feldspar in deformed granitoids and its relationship to the distribution of water: Tectonophysics, v. 532–535, p. 175–185, https://doi.org/10.1016/j.tecto.2012.01.033.
Fusseis, F., and Handy, M.R., 2008, Micromechanisms of shear zone propagation at the brittle-viscous transition: Journal of Structural Geology, v. 30, p. 1242–1253, https://doi.org/10.1016/j.jsg.2008.06.005.
Fusseis, F., Regenauer-Lieb, K., Liu, J., Hough, R.M., and De Carlo, F., 2009, Creep cavitation can establish a dynamic granular fluid pump in ductile shear zones: Nature, v. 459, p. 974–977, https://doi.org/10.1038/nature08051.
Gan, W., Zhang, P., Shen, Z.K., Niu, Z., Wang, M., Wan, Y., Zhou, D., and Cheng, J., 2007, Present-day crustal motion within the Tibetan Plateau inferred from GPS measurements: Journal of Geophysical Research, v. 112, B08416, https://doi.org/10.1029/2005JB004120.
Ghent, E.D., and Stout, M.Z., 1984, TiO_2 activity in metamorphosed pelitic and basic rocks: Principles and applications to metamorphism in southeastern Canadian Cordillera: Contributions to Mineralogy and Petrology, v. 86, p. 248–255, https://doi.org/10.1007/BF00373670.
Giovanni, M.K., 2007, Tectonic and thermal evolution of the Cordillera Blanca detachment system, Peruvian Andes: Implications for normal faulting in a contractional orogen [Ph.D. thesis]: Los Angeles, University of California Los Angeles, 237 p.
Giovanni, M.K., Horton, B.K., Garzione, C.N., McNulty, B., and Grove, M., 2010, Extensional basin evolution in the Cordillera Blanca, Peru: Stratigraphic and isotopic records of detachment faulting and orogenic collapse in the Andean hinterland: Tectonics, v. 29, TC6007, https://doi.org/10.1029/2010TC002666.
Goscombe, B.D., Passchier, C.W., and Hand, M., 2004, Boudinage classification: End-member boudin types and modified boudin structures: Journal of Structural Geology, v. 26, p. 739–763, https://doi.org/10.1016/j.jsg.2003.08.015.
Gottardi, R., and Teyssier, C., 2013, Thermomechanics of an extensional shear zone, Raft River metamorphic core complex, NW Utah: Journal of Structural Geology, v. 53, p. 54–69, https://doi.org/10.1016/j.jsg.2013.05.012.
Grujic, D., Stipp, M., and Wooden, J.L., 2011, Thermometry of quartz mylonites: Importance of dynamic recrystallization on Ti-in-quartz reequilibration: Geochemistry Geophysics Geosystems, v. 12, Q06012, https://doi.org/10.1029/2010GC003368.
Gutscher, M.-A., Olivet, J.-L., Aslanian, D., Eissen, J.-P., and Maury, R., 1999, The "lost Inca Plateau": Cause of flat subduction beneath Peru?: Earth and Planetary Science Letters, v. 171, p. 335–341, https://doi.org/10.1016/S0012-821X(99)00153-3.
Hacker, B.R., Yin, A., Christie, J.M., and Snoke, A.W., 1990, Differential stress, strain rate, and temperatures of mylonitization in the Ruby Mountains, Nevada: Implications for the rate and duration of uplift: Journal of Geophysical Research, v. 95, p. 8569–8580, https://doi.org/10.1029/JB095iB06p08569.
Haertel, M., and Herwegh, M., 2014, Microfabric memory of vein quartz for strain localization in detachment faults: A case study on the Simplon fault zone: Journal of Structural Geology, v. 68, p. 16–32, https://doi.org/10.1016/j.jsg.2014.08.001.
Haertel, M., Herwegh, M., and Pettke, T., 2013, Titanium-in-quartz thermometry on synkinematic quartz veins in a retrograde crustal-scale normal fault zone: Tectonophysics, v. 608, p. 468–481, https://doi.org/10.1016/j.tecto.2013.08.042.
Halfpenny, A., Prior, D.J., and Wheeler, J., 2006, Analysis of dynamic recrystallization and nucleation in a quartzite mylonite: Tectonophysics, v. 427, p. 3–14, https://doi.org/10.1016/j.tecto.2006.05.016.
Halfpenny, A., Prior, D.J., and Wheeler, J., 2012, Electron backscatter diffraction analysis to determine the mechanisms that operated during dynamic recrystallisation of quartz-rich rocks: Journal of Structural Geology, v. 36, p. 2–15, https://doi.org/10.1016/j.jsg.2012.01.001.
Handy, M.R., Wissing, S.B., and Streit, L.E., 1999, Frictional-viscous flow in mylonite with varied bimineralic composition and its effect on lithospheric strength: Tectonophysics, v. 303, p. 175–191, https://doi.org/10.1016/S0040-1951(98)00251-0.
Hayden, L.A., and Watson, E.B., 2007, Rutile saturation in hydrous siliceous melts and its bearing on Ti-thermometry of quartz and zircon: Earth and Planetary Science Letters, v. 258, p. 561–568, https://doi.org/10.1016/j.epsl.2007.04.020.
Heilbronner, R., and Tullis, J., 2006, Evolution of c axis pole figures and grain size during dynamic recrystallization: Results from experimentally sheared quartzite: Journal of Geophysical Research, v. 111, B10202, https://doi.org/10.1029/2005JB004194.
Hippertt, J.F.M., 1993, 'V'-pull-apart microstructures: A new shear-sense indicator: Journal of Structural Geology, v. 15, p. 1393–1403, https://doi.org/10.1016/0191-8141(93)90001-Q.
Hippertt, J.F.M., 1998, Breakdown of feldspar, volume gain and lateral mass transfer during mylonitization of granitoid in a low metamorphic grade shear zone: Journal of Structural Geology, v. 20, p. 175–193, https://doi.org/10.1016/S0191-8141(97)00083-7.
Hirth, G., and Tullis, J., 1992, Dislocation creep regimes in quartz aggregates: Journal of Structural Geology, v. 14, p. 145–159, https://doi.org/10.1016/0191-8141(92)90053-Y.
Hirth, G., and Tullis, J., 1994, The brittle-plastic transition in experimentally deformed quartz aggregates: Journal of Geophysical Research, v. 99, p. 11,731–11,747, https://doi.org/10.1029/93JB02873.
Hirth, G., Teyssier, C., and Dunlap, W.J., 2001, An evaluation of quartzite flow laws based on comparisons between experimentally and naturally deformed rocks: International Journal of Earth Sciences, v. 90, p. 77–87, https://doi.org/10.1007/s005310000152.
Holyoke, C.W., III, and Kronenberg, A.K., 2010, Accurate differential stress measurement using the molten salt cell and solid salt assemblies in the Griggs apparatus with applications to strength, piezometers and rheology: Tectonophysics, v. 494, p. 17–31, https://doi.org/10.1016/j.tecto.2010.08.001.
Holyoke, C.W., III, and Tullis, J., 2006, The interaction between reaction and deformation: An experimental study using a biotite + plagioclase + quartz gneiss: Journal of Metamorphic Geology, v. 24, p. 743–762, https://doi.org/10.1111/j.1525-1314.2006.00666.x.
Huang, R., and Audétat, A., 2012, The titanium-in-quartz (TitaniQ) thermobarometer: A critical examination and re-calibration: Geochimica et Cosmochimica Acta, v. 84, p. 75–89, https://doi.org/10.1016/j.gca.2012.01.009.
Ishii, K., Kanagawa, K., Shigematsu, N., and Okudaira, T., 2007, High ductility of K-feldspar and development of granitic banded ultramylonite in the Ryoke metamorphic belt, SW Japan: Journal of Structural Geology, v. 29, p. 1083–1098, https://doi.org/10.1016/j.jsg.2007.02.008.
James, D.E., 1971, Plate tectonic model for the evolution of the Central Andes: Geological Society of America Bulletin, v. 82, p. 3325–3346, https://doi.org/10.1130/0016-7606(1971)82[3325:PTMFTE]2.0.CO;2.
Jiang, Z., Prior, D.J., and Wheeler, J., 2000, Albite crystallographic preferred orientation and grain misorientation distribution in a low-grade mylonite: Implications for granular flow: Journal of Structural Geology, v. 22, p. 1663–1674, https://doi.org/10.1016/S0191-8141(00)00079-1.
Jordan, T.E., Isacks, B.L., Allmendinger, R.W., Brewer, J.A., Ramos, V.A., and Ando, C.J., 1983, Andean tectonics related to geometry of subducted Nazca plate: Geological Society of America Bulletin, v. 94, p. 341–361, https://doi.org/10.1130/0016-7606(1983)94<341:ATRTGO>2.0.CO;2.
Keller, L.M., and Stipp, M., 2011, The single-slip hypothesis revisited: Crystal-preferred orientations of sheared quartz aggregates with increasing strain in nature and numerical simulation: Journal of Structural Geology, v. 33, p. 1491–1500, https://doi.org/10.1016/j.jsg.2011.07.008.
Kidder, S., Avouac, J.-P., and Chan, Y.-C., 2013, Application of titanium-in-quartz thermobarometry to greenschist facies veins and recrystallized quartzites in the Hsüehshan range, Taiwan: Solid Earth, v. 4, p. 1–21, https://doi.org/10.5194/se-4-1-2013.
Kilian, R., Heilbronner, R.P., and Stünitz, H., 2011, Quartz grain size reduction in a granitoid rock and the transition from dislocation to diffusion creep: Journal of Structural Geology, v. 33, p. 1265–1284, https://doi.org/10.1016/j.jsg.2011.05.004.
Kirby, S.H., 1980, Tectonic stresses in the lithosphere: Constraints provided by the experimental deformation of rocks: Journal of Geophysical Research, v. 85, p. 6353–6363, https://doi.org/10.1029/JB085iB11p06353.
Kirby, S.H., 1983, Rheology of the lithosphere: Reviews of Geophysics and Space Physics, v. 21, p. 1458–1487, https://doi.org/10.1029/RG021i006p01458.
Kruhl, J.H., 1996, Prism- and basal-plane parallel subgrain boundaries in quartz: A microstructural geothermobarometer: Journal of Metamorphic Geology, v. 14, p. 581–589, https://doi.org/10.1046/j.1525-1314.1996.00413.x.
Kularatne, K., and Audétat, A., 2014, Rutile solubility in hydrous rhyolite melts at 750–900 °C and 2 kbar, with application to titanium-in-quartz (TitaniQ) thermobarometry: Geochimica et Cosmochimica Acta, v. 125, p. 196–209, https://doi.org/10.1016/j.gca.2013.10.020.
Langille, J.M., Jessup, M.J., Cottle, J.M., Newell, D.L., and Seward, G., 2010, Kinematic evolution of the Ama Drime detachment: Insights into orogen-parallel extension and exhumation of the Ama Drime Massif, Tibet–Nepal: Journal of Structural Geology, v. 32, p. 900–919, https://doi.org/10.1016/j.jsg.2010.04.005.
Law, R.D., 2014, Deformation thermometry based on quartz *c*-axis fabrics and recrystallization microstructures: A review: Journal of Structural Geology, v. 66, p. 129–161, https://doi.org/10.1016/j.jsg.2014.05.023.

Law, R.D., Schmid, S.M., and Wheeler, J., 1990, Simple shear deformation and quartz crystallographic fabrics: A possible natural example from the Torridon area of NW Scotland: Journal of Structural Geology, v. 12, p. 29–45, https://doi.org/10.1016/0191-8141(90)90046-2.

Lister, G.S., and Hobbs, B.E., 1980, The simulation of fabric development during plastic deformation and its application to quartzite: The influence of deformation history: Journal of Structural Geology, v. 2, p. 355–370, https://doi.org/10.1016/0191-8141(80)90023-1.

Lister, G.S., and Snoke, A.W., 1984, S-C mylonites: Journal of Structural Geology, v. 6, p. 617–638, https://doi.org/10.1016/0191-8141(84)90001-4.

Lloyd, G.E., Law, R.D., Mainprice, D.H., and Wheeler, J., 1992, Microstructural and crystal fabric evolution during shear zone formation: Journal of Structural Geology, v. 14, p. 1079–1100, https://doi.org/10.1016/0191-8141(92)90037-W.

Mainprice, D.H., and Paterson, M.S., 1984, Experimental studies of the role of water in the plasticity of quartzites: Journal of Geophysical Research, v. 89, p. 4257–4269, https://doi.org/10.1029/JB089iB06p04257.

Mainprice, D.H., Bouchez, J.-L., Blumenfeld, P., and Tubià, J.M., 1986, Dominant *c* slip in naturally deformed quartz: Implications for dramatic plastic softening at high temperature: Geology, v. 14, p. 819–822, https://doi.org/10.1130/0091-7613(1986)14<819:DCSIND>2.0.CO;2.

Mancktelow, N.S., and Pennacchioni, G., 2004, The influence of grain boundary fluids on the microstructure of quartz-feldspar mylonites: Journal of Structural Geology, v. 26, p. 47–69, https://doi.org/10.1016/S0191-8141(03)00081-6.

Margirier, A., Robert, X., Audin, L., Gautheron, C., Bernet, M., Hall, S., and Simon-Labric, T., 2015, Slab flattening, magmatism, and surface uplift in the Cordillera Occidental (Northern Peru): Geology, v. 43, p. 1031–1034, https://doi.org/10.1130/G37061.1.

Margirier, A., Audin, L., Robert, X., Herman, F., Ganne, J., and Schwartz, S., 2016, Time and mode of exhumation of the Cordillera Blanca batholith (Peruvian Andes): Journal of Geophysical Research: Solid Earth, v. 121, p. 6235–6249, https://doi.org/10.1002/2016JB013055.

McLaren, A.C., and Pryer, L.L., 2001, Microstructural investigation of the interaction and interdependence of cataclastic and plastic mechanisms in feldspar crystals deformed in the semi-brittle field: Tectonophysics, v. 335, p. 1–15, https://doi.org/10.1016/S0040-1951(01)00042-7.

McNulty, B., and Farber, D., 2002, Active detachment faulting above the Peruvian flat slab: Geology, v. 30, p. 567–570, https://doi.org/10.1130/0091-7613(2002)030<0567:ADFATP>2.0.CO;2.

McNulty, B.A., Farber, D.L., Wallace, G.S., Lopez, R., and Palacios, O., 1998, Role of plate kinematics and plate-slip-vector partitioning in continental magmatic arcs: Evidence from the Cordillera Blanca, Peru: Geology, v. 26, p. 827–830, https://doi.org/10.1130/0091-7613(1998)026<0827:ROPKAP>2.3.CO;2.

Menegon, L., Pennacchioni, G., and Stünitz, H., 2006, Nucleation and growth of myrmekite during ductile shear deformation in metagranites: Journal of Metamorphic Geology, v. 24, p. 553–568, https://doi.org/10.1111/j.1525-1314.2006.00654.x.

Menegon, L., Pennacchioni, G., and Spiess, R., 2008, Dissolution-precipitation creep of K-feldspar in mid-crustal granite mylonites: Journal of Structural Geology, v. 30, p. 565–579, https://doi.org/10.1016/j.jsg.2008.02.001.

Menegon, L., Fusseis, F., Stünitz, H., and Xiao, X., 2015, Creep cavitation bands control porosity and fluid flow in lower crustal shear zones: Geology, v. 43, p. 227–230, https://doi.org/10.1130/G36307.1.

Miranda, E.A., Hirth, G., and John, B.E., 2016, Microstructural evidence for the transition from dislocation creep to dislocation-accommodated grain boundary sliding in naturally deformed plagioclase: Journal of Structural Geology, v. 92, p. 30–45, https://doi.org/10.1016/j.jsg.2016.09.002.

Morales, L.F.G., Mainprice, D.H., Lloyd, G.E., and Law, R.D., 2011, Crystal fabric development and slip systems in a quartz mylonite: An approach via transmission electron microscopy and viscoplastic self-consistent modelling, *in* Prior, D.J., Rutter, E.H., and Tatham, D.J., eds., Deformation Mechanisms, Rheology and Tectonics: Microstructures, Mechanics and Anisotropy: Geological Society of London Special Publication 360, p. 151–174, https://doi.org/10.1144/SP360.9.

Morales, L.F.G., Lloyd, G.E., and Mainprice, D., 2014, Fabric transitions in quartz via viscoplastic self-consistent modeling part I: Axial compression and simple shear under constant strain: Tectonophysics, v. 636, p. 52–69, https://doi.org/10.1016/j.tecto.2014.08.011.

Mukasa, S.B., 1984, Comparative Pb isotope systematics and zircon U-Pb geochronology for the Coastal, San Nicolás, and Cordillera Blanca batholiths, Peru [Ph.D. thesis]: Santa Barbara, University of California, Santa Barbara, 148 p.

Nachlas, W.O., and Hirth, G., 2015, Experimental constraints on the role of dynamic recrystallization on resetting the Ti-in-quartz thermobarometer: Journal of Geophysical Research: Solid Earth, v. 120, p. 8120–8137, https://doi.org/10.1002/2015JB012274.

Nachlas, W.O., Whitney, D.L., Teyssier, C., Bagley, B., and Mulch, A., 2014, Titanium concentration in quartz as a record of multiple deformation mechanisms in an extensional shear zone: Geochemistry Geophysics Geosystems, v. 15, p. 1374–1397, https://doi.org/10.1002/2013GC005200.

Nachlas, W.O., Thomas, J.B., and Hirth, G., 2018, TitaniQ deformed: Experimental deformation of out-of-equilibrium quartz porphyroclasts: Journal of Structural Geology, v. 116, p. 207–222, https://doi.org/10.1016/j.jsg.2018.07.012.

Newell, D.L., Jessup, M.J., Hilton, D.R., Shaw, C.A., and Hughes, C.A., 2015, Mantle-derived helium in hot springs of the Cordillera Blanca, Peru: Implications for mantle-to-crust fluid transfer in a flat-slab subduction setting: Chemical Geology, v. 417, p. 200–209, https://doi.org/10.1016/j.chemgeo.2015.10.003.

Oliot, E., Goncalves, P., Schulmann, K., Marquer, D., and Lexa, O., 2014, Mid-crustal shear zone formation in granitic rocks: Constraints from quantitative textural and crystallographic preferred orientations analyses: Tectonophysics, v. 612–613, p. 63–80, https://doi.org/10.1016/j.tecto.2013.11.032.

Passchier, C.W., and Trouw, R.A.J., 2005, Microtectonics: Berlin, Heidelberg, Springer-Verlag, 366 p., https://doi.org/10.1007/3-540-29359-0.

Paterson, S.R., Vernon, R.H., and Tobisch, O.T., 1989, A review of criteria for the identification of magmatic and tectonic foliations in granitoids: Journal of Structural Geology, v. 11, p. 349–363, https://doi.org/10.1016/0191-8141(89)90074-6.

Pennacchioni, G., Di Toro, G., Brack, P., Menegon, L., and Villa, I.M., 2006, Brittle-ductile-brittle deformation during cooling of tonalite (Adamello, Southern Italian Alps): Tectonophysics, v. 427, p. 171–197, https://doi.org/10.1016/j.tecto.2006.05.019.

Pennacchioni, G., Menegon, L., Leiss, B., Nestola, F., and Bromiley, G., 2010, Development of crystallographic preferred orientation and microstructure during plastic deformation of natural coarse-grained quartz veins: Journal of Geophysical Research, v. 115, B12405, https://doi.org/10.1029/2010JB007674.

Peterman, E.M., and Grove, M., 2010, Growth conditions of symplectic muscovite + quartz: Implications for quantifying retrograde metamorphism in exhumed magmatic arcs: Geology, v. 38, p. 1071–1074, https://doi.org/10.1130/G31449.1.

Petford, N., and Atherton, M.P., 1992, Granitoid emplacement and deformation along a major crustal lineament: The Cordillera Blanca, Peru: Tectonophysics, v. 205, p. 171–185, https://doi.org/10.1016/0040-1951(92)90425-6.

Petford, N., and Atherton, M., 1996, Na-rich partial melts from newly underplated basaltic crust: The Cordillera Blanca Batholith, Peru: Journal of Petrology, v. 37, p. 1491–1521, https://doi.org/10.1093/petrology/37.6.1491.

Pfiffner, O.A., and Gonzalez, L., 2013, Mesozoic–Cenozoic Evolution of the Western Margin of South America: Case Study of the Peruvian Andes: Geosciences, v. 3, p. 262–310, https://doi.org/10.3390/geosciences3020262.

Phillips, E.R., Ransom, D.M., and Vernon, R.H., 1972, Myrmekite and muscovite developed by retrograde metamorphism at Broken Hill, New South Wales: Mineralogical Magazine, v. 38, p. 570–578, https://doi.org/10.1180/minmag.1972.038.297.05.

Platt, J.P., 2015, Rheology of two-phase systems: A microphysical and observational approach: Journal of Structural Geology, v. 77, p. 213–227, https://doi.org/10.1016/j.jsg.2015.05.003.

Platt, J.P., and Behr, W.M., 2011a, Grainsize evolution in ductile shear zones: Implications for strain localization and the strength of the lithosphere: Journal of Structural Geology, v. 33, p. 537–550, https://doi.org/10.1016/j.jsg.2011.01.018.

Platt, J.P., and Behr, W.M., 2011b, Lithospheric shear zones as constant stress experiments: Geology, v. 39, p. 127–130, https://doi.org/10.1130/G31561.1.

Pryer, L.L., 1993, Microstructures in feldspars from a major crustal thrust zone: The Grenville Front, Ontario, Canada: Journal of Structural Geology, v. 15, p. 21–36, https://doi.org/10.1016/0191-8141(93)90076-M.

Rahl, J.M., and Skemer, P., 2016, Microstructural evolution and rheology of quartz in a mid-crustal shear zone: Tectonophysics, v. 680, p. 129–139, https://doi.org/10.1016/j.tecto.2016.05.022.

Ramos, V.A., 1999, Plate tectonic setting of the Andean Cordillera: Episodes, v. 22, p. 183–190.

Ree, J.H., Kim, H.S., Han, R., and Jung, H., 2005, Grain-size reduction of feldspars by fracturing and neocrystallization in a low-grade granitic mylonite and its rheological effect: Tectonophysics, v. 407, p. 227–237, https://doi.org/10.1016/j.tecto.2005.07.010.

Rosenberg, C.L., 2001, Deformation of partially molten granite: A review and comparison of experimental and natural case studies: International Journal of Earth Sciences, v. 90, p. 60–76, https://doi.org/10.1007/s005310000164.

Rosenberg, C.L., and Handy, M.R., 2005, Experimental deformation of partially melted granite revisited: Implications for the continental crust: Journal of Metamorphic Geology, v. 23, p. 19–28, https://doi.org/10.1111/j.1525-1314.2005.00555.x.

Rutter, E.H., 1986, On the nomenclature of mode of failure transitions in rocks: Tectonophysics, v. 122, p. 381–387, https://doi.org/10.1016/0040-1951(86)90153-8.

Rutter, E.H., and Brodie, K.H., 2004, Experimental intracrystalline plastic flow in hot-pressed synthetic quartzite prepared from Brazilian quartz crystals: Journal of Structural Geology, v. 26, p. 259–270, https://doi.org/10.1016/S0191-8141(03)00096-8.

Rutter, E.H., Holdsworth, R.E.., and Knipe, R.J., 2001, The nature and tectonic significance of fault-zone weakening: An introduction, *in* Holdsworth, R.E., Strachan, R.A., Magloughlin, J.F., and Knipe, R.J., eds., The Nature and Tectonic Significance of Fault Zone Weakening: Geological Society of London Special Publication 186, p. 1–11, https://doi.org/10.1144/GSL.SP.2001.186.01.01.

Samanta, S.K., Mandal, N., and Chakraborty, C., 2002, Development of different types of pull-apart microstructures in mylonites: An experimental investigation: Journal of Structural Geology, v. 24, p. 1345–1355, https://doi.org/10.1016/S0191-8141(01)00139-0.

Scherrenberg, A.F., Holcombe, R.J., and Rosenbaum, G., 2014, The persistence and role of basin structures on the 3D architecture of the Marañón Fold-Thrust Belt, Peru: Journal of South American Earth Sciences, v. 51, p. 45–58, https://doi.org/10.1016/j.jsames.2013.12.007.

Scherrenberg, A.F., Kohn, B.P., Holcombe, R.J., and Rosenbaum, G., 2016, Thermotectonic history of the Marañón Fold-Thrust Belt, Peru: Insights into mineralisation in an evolving orogen: Tectonophysics, v. 667, p. 16–36, https://doi.org/10.1016/j.tecto.2015.11.007.

Schmid, S.M., and Casey, M., 1986, Complete fabric analysis of some commonly observed quartz c-axis patterns, *in* Hobbs, B.E., and Heard, H.C., eds., Mineral and Rock Deformation: Laboratory Studies: American Geophysical Union Geophysical Monograph 36, p. 263–286, https://doi.org/10.1029/GM036p0263.

Schwartz, D.P., 1988, Paleoseismicity and neotectonics of the Cordillera Blanca Fault Zone, northern Peruvian Andes: Journal of Geophysical Research, v. 93, p. 4712–4730, https://doi.org/10.1029/JB093iB05p04712.

Siame, L.L., Sébrier, M., Bellier, O., and Bourles, D., 2006, Can cosmic ray exposure dating reveal the normal faulting activity of the Cordillera Blanca Fault, Peru?: Revista de la Asociación Geológica Argentina, v. 61, p. 536–544.

Sibson, R.H., 1983, Continental fault structure and the shallow earthquake source: Journal of the Geological Society, v. 140, p. 741–767, https://doi.org/10.1144/gsjgs.140.5.0741.

Simpson, C., 1985, Deformation of granitic rocks across the brittle-ductile transition: Journal of Structural Geology, v. 7, p. 503–511, https://doi.org/10.1016/0191-8141(85)90023-9.

Simpson, C., and Wintsch, R.P., 1989, Evidence for deformation-induced K-feldspar replacement by myrmekite: Journal of Metamorphic Geology, v. 7, p. 261–275, https://doi.org/10.1111/j.1525-1314.1989.tb00588.x.

Singleton, J.S., and Mosher, S., 2012, Mylonitization in the lower plate of the Buckskin-Rawhide detachment fault, west-central Arizona: Implications for the geometric evolution of metamorphic core complexes: Journal of Structural Geology, v. 39, p. 180–198, https://doi.org/10.1016/j.jsg.2012.02.013.

Skemer, P., Katayama, I., Jiang, Z., and Karato, S., 2005, The misorientation index: Development of a new method for calculating the strength of lattice-preferred orientation: Tectonophysics, v. 411, p. 157–167, https://doi.org/10.1016/j.tecto.2005.08.023.

Spruzeniece, L., and Piazolo, S., 2015, Strain localization in brittle-ductile shear zones: Fluid-abundant vs. fluid-limited conditions (an example from Wyangala area, Australia): Solid Earth, v. 6, p. 881–901, https://doi.org/10.5194/se-6-881-2015.

Sterner, S.M., and Pitzer, K.S., 1994, An equation of state for carbon dioxide valid from zero to extreme pressures: Contributions to Mineralogy and Petrology, v. 117, p. 362–374, https://doi.org/10.1007/BF00307271.

Stipp, M., and Tullis, J., 2003, The recrystallized grain size piezometer for quartz: Geophysical Research Letters, v. 30, 2088, https://doi.org/10.1029/2003GL018444.

Stipp, M., Stünitz, H., Heilbronner, R.P., and Schmid, S.M., 2002a, Dynamic recrystallization of quartz: Correlation between natural and experimental conditions, *in* De Meer, S., Drury, M.R., De Bresser, J.H.P., and Pennock, G.M., eds., Deformation Mechanisms, Rheology and Tectonics: Status and Future Perspectives: Geological Society of London Special Publication 200, p. 171–190, https://doi.org/10.1144/GSL.SP.2001.200.01.11.

Stipp, M., Stünitz, H., Heilbronner, R.P., and Schmid, S.M., 2002b, The eastern Tonale fault zone: A "natural laboratory" for crystal plastic deformation of quartz over a temperature range from 250 to 700 °C: Journal of Structural Geology, v. 24, p. 1861–1884, https://doi.org/10.1016/S0191-8141(02)00035-4.

Stipp, M., Tullis, J., and Behrens, H., 2006, Effect of water on the dislocation creep microstructure and flow stress of quartz and implications for the recrystallized grain size piezometer: Journal of Geophysical Research, v. 111, B04201, https://doi.org/10.1029/2005JB003852.

Storey, C.D., and Prior, D.J., 2005, Plastic deformation and recrystallization of garnet: A mechanism to facilitate diffusion creep: Journal of Petrology, v. 46, p. 2593–2613, https://doi.org/10.1093/petrology/egi067.

Stormer, J.C., Jr., 1975, A practical two-feldspar geothermometer: American Mineralogist, v. 60, p. 667–674.

Stünitz, H., and Fitz Gerald, J.D., 1993, Deformation of granitoids at low metamorphic grade. II: Granular flow in albite-rich mylonites: Tectonophysics, v. 221, p. 299–324, https://doi.org/10.1016/0040-1951(93)90164-F.

Stünitz, H., and Tullis, J., 2001, Weakening and strain localization produced by syn-deformational reaction of plagioclase: International Journal of Earth Sciences, v. 90, p. 136–148, https://doi.org/10.1007/s005310000148.

Stünitz, H., Fitz Gerald, J.D., and Tullis, J., 2003, Dislocation generation, slip systems, and dynamic recrystallization in experimentally deformed plagioclase single crystals: Tectonophysics, v. 372, p. 215–233, https://doi.org/10.1016/S0040-1951(03)00241-5.

Sullivan, W.A., Boyd, A.S., and Monz, M.E., 2013, Strain localization in homogeneous granite near the brittle-ductile transition: A case study of the Kellyland fault zone, Maine, USA: Journal of Structural Geology, v. 56, p. 70–88, https://doi.org/10.1016/j.jsg.2013.09.003.

Thomas, J.B., and Watson, E.B., 2012, Application of the Ti-in-quartz thermobarometer to rutile-free systems. Reply to: A comment on: "TitaniQ under pressure: The effect of pressure and temperature on the solubility of Ti in quartz" by Thomas et al.: Contributions to Mineralogy and Petrology, v. 164, p. 369–374, https://doi.org/10.1007/s00410-012-0761-5.

Thomas, J.B., Watson, E.B., Spear, F.S., Shemella, P.T., Nayak, S.K., and Lanzirotti, A., 2010, TitaniQ under pressure: The effect of pressure and temperature on the solubility of Ti in quartz: Contributions to Mineralogy and Petrology, v. 160, p. 743–759, https://doi.org/10.1007/s00410-010-0505-3.

Tokle, L., Hirth, G., and Behr, W.M., 2019, Flow laws and fabric transitions in wet quartzite: Earth and Planetary Science Letters, v. 505, p. 152–161, https://doi.org/10.1016/j.epsl.2018.10.01.

Toy, V.G., Prior, D.J., and Norris, R.J., 2008, Quartz fabrics in the Alpine Fault mylonites: Influence of pre-existing preferred orientations on fabric development during progressive uplift: Journal of Structural Geology, v. 30, p. 602–621, https://doi.org/10.1016/j.jsg.2008.01.001.

Tsurumi, J., Hosonuma, H., and Kanagawa, K., 2002, Strain localization due to a positive feedback of deformation and myrmekite-forming reaction in granite and aplite mylonites along the Hatagawa Shear Zone of NE Japan: Journal of Structural Geology, v. 25, p. 557–574, https://doi.org/10.1016/S0191-8141(02)00048-2.

Tullis, J., and Yund, R.A., 1977, Experimental deformation of dry Westerly granite: Journal of Geophysical Research, v. 82, p. 5705–5718, https://doi.org/10.1029/JB082i036p05705.

Tullis, J., and Yund, R.A., 1980, Hydrolytic weakening of experimentally deformed Westerly granite and Hale albite rock: Journal of Structural Geology, v. 2, p. 439–451, https://doi.org/10.1016/0191-8141(80)90005-X.

Tullis, J., and Yund, R.A., 1985, Dynamic recrystallization of feldspar: A mechanism for ductile shear zone formation: Geology, v. 13, p. 238, https://doi.org/10.1130/0091-7613(1985)13<238:DROFAM>2.0.CO;2.

Tullis, J., and Yund, R.A., 1987, Transition from cataclastic flow to dislocation creep of feldspar: Mechanisms and microstructures: Geology, v. 15, p. 606–609, https://doi.org/10.1130/0091-7613(1987)15<606:TFCFTD>2.0.CO;2.

Tullis, J., and Yund, R.A., 1991, Diffusion creep in feldspar aggregates: Experimental evidence: Journal of Structural Geology, v. 13, p. 987–1000, https://doi.org/10.1016/0191-8141(91)90051-J.

Tullis, J., Christie, J.M., and Griggs, D.T., 1973, Microstructures and preferred orientations of experimentally deformed quartzites: Geological Society of America Bulletin, v. 84, p. 297–314, https://doi.org/10.1130/0016-7606(1973)84<297:MAPOOE>2.0.CO;2.

Twiss, R.J., 1977, Theory and applicability of a recrystallized grain-size paleopiezometer: Pure and Applied Geophysics, v. 115, p. 227–244, https://doi.org/10.1007/BF01637105.

Viegas, G., Menegon, L., and Archanjo, C., 2016, Brittle grain-size reduction of feldspar, phase mixing and strain localization in granitoids at mid-crustal conditions (Pernambuco shear zone, NE Brazil): Solid Earth, v. 7, p. 375–396, https://doi.org/10.5194/se-7-375-2016.

Wark, D.A., and Watson, E.B., 2006, TitaniQ: A titanium-in-quartz geothermometer: Contributions to Mineralogy and Petrology, v. 152, p. 743–754, https://doi.org/10.1007/s00410-006-0132-1.

Warren, J.M., and Hirth, G., 2006, Grain size sensitive deformation mechanisms in naturally deformed peridotites: Earth and Planetary Science Letters, v. 248, p. 438–450, https://doi.org/10.1016/j.epsl.2006.06.006.
Wehrens, P., Berger, A., Peters, M., Spillmann, T., and Herwegh, M., 2016, Deformation at the frictional-viscous transition: Evidence for cycles of fluid-assisted embrittlement and ductile deformation in the granitoid crust: Tectonophysics, v. 693, p. 66–84, https://doi.org/10.1016/j.tecto.2016.10.022.
Wells, M.L., Beyene, M.A., Spell, T.L., Kula, J.L., Miller, D.M., and Zanetti, K.A., 2005, The Pinto shear zone: A Laramide synconvergent extensional shear zone in the Mojave Desert region of the southwestern United States: Journal of Structural Geology, v. 27, p. 1697–1720, https://doi.org/10.1016/j.jsg.2005.03.005.
Whitney, J.A., and Stormer, J.C., Jr., 1977, The distribution of $NaAlSi_3O_8$ between coexisting microcline and plagioclase and its effect on geothermometric calculations: American Mineralogist, v. 62, p. 687–691.
Wightman, R.H., Prior, D.J., and Little, T.A., 2006, Quartz veins deformed by diffusion creep-accommodated grain boundary sliding during a transient, high strain-rate event in the Southern Alps, New Zealand: Journal of Structural Geology, v. 28, p. 902–918, https://doi.org/10.1016/j.jsg.2006.02.008.
Wilson, P.A., 1975, Potassium-argon age studies in Peru with particular reference to the chronology of emplacement of the Coastal batholith [Ph.D. thesis]: Liverpool, UK, University of Liverpool, 299 p.
Wintsch, R.P., and Yeh, M.-W., 2013, Oscillating brittle and viscous behavior through the earthquake cycle in the Red River Shear Zone: Monitoring flips between reaction and textural softening and hardening: Tectonophysics, v. 587, p. 46–62, https://doi.org/10.1016/j.tecto.2012.09.019.
Wise, J.M., and Noble, D.C., 2003, Geomorphic evolution of the Cordillera Blanca, northern Peru: Boletín de la Sociedad Geológica del Perú, v. 96, p. 65–85.
Yund, R.A., and Tullis, J., 1980, The effect of water, pressure, and strain on Ai/Si order-disorder kinetics in feldspar: Contributions to Mineralogy and Petrology, v. 72, p. 297–302, https://doi.org/10.1007/BF00376148.
Zibra, I., Kruhl, J.H., Montanini, A., and Tribuzio, R., 2012, Shearing of magma along a high-grade shear zone: Evolution of microstructures during the transition from magmatic to solid-state flow: Journal of Structural Geology, v. 37, p. 150–160, https://doi.org/10.1016/j.jsg.2012.01.011.